Prediction of Highly Selective Electrocatalytic Nitrogen Reduction at Low Overpotential on a Mo-doped g-GaN Monolayer

Lesheng Li,[†] J. Mark P. Martirez,[‡] and Emily A. Carter[*,†,‡,∥]

[†]Department of Mechanical and Aerospace Engineering, Princeton University, Princeton, NJ 08544-5263, United States and [‡]Department of Chemical and Biomolecular Engineering, and [∥]Office of the Chancellor, Box 951405, University of California, Los Angeles, Los Angeles, CA 90095-1405, United States

KEYWORDS Nitrogen reduction reaction, single-atom catalysts, gallium nitride monolayer, selectivity, density functional theory calculations

ABSTRACT: Identifying efficient electrocatalysts with low overpotential and high selectivity for producing ammonia from nitrogen gas is essential for any future electrocatalytic nitrogen reduction reaction (NRR) based ammonia synthesis. Via density functional theory calculations and the computational hydrogen electrode model, we systematically examine the prospect of using a single-transition-metal (TM)-atom-doped graphene-like GaN (g-GaN) monolayer as an electrocatalyst for artificial nitrogen reduction. Among 15 TMs investigated, the Mo-doped g-GaN (Mo@g-GaN) monolayer is the only electrocatalyst predicted to be feasible for the NRR. The Mo@g-GaN monolayer satisfies all screening criteria considered for activating the inert N≡N triple bond effectively, including stabilization of the adsorbed (*) NRR intermediate *NNH and destabilization of the *NH_2 species. This monolayer also possesses sufficient overall stability. A complete analysis of the likely mechanisms involved in the NRR on this catalyst suggests that the Mo@g-GaN monolayer could exhibit promising NRR catalytic activity. It achieves this via one specific (distal) pathway, which has a very low onset potential of -0.33 V vs. the reversible hydrogen electrode (RHE), corresponding to a low overpotential of 0.42 V vs. the RHE, defined using the measured equilibrium potential for NRR of 0.09 V vs. the RHE. The potential-determining step, conversion of *NH_2 to *NH_3, also exhibits a surmountable barrier of 0.42 eV, suggesting kinetics will be facile. Finally, the Mo@g-GaN monolayer is predicted to exhibit substantial selectivity (~31%) toward ammonia synthesis over the competing hydrogen evolution reaction. These findings may open a potential route for artificial ammonia synthesis using a single-atom catalyst under ambient conditions.

1. INTRODUCTION

Artificial ammonia (NH_3) synthesis is of great significance because it is a fundamental component in the global economy. Ammonia is not only the primary precursor to produce fertilizers, pharmaceuticals, and explosives[1-3] but it also is a promising energy carrier due to its high energy density.[4-6] However, conversion of nitrogen (N_2) to NH_3 under ambient conditions remains a major engineering challenge. This is because of the very strong N≡N triple bond that renders the N_2 molecule extremely stable and therefore very difficult to activate.[7-8]

Artificial nitrogen fixation to ammonia presently relies primarily on the century-old Haber-Bosch (HB) process. Although this industrial process exhibits exceptional efficiency and currently contributes almost 90% of annual NH_3 production,[9-10] it requires high temperatures (~500 ºC) and pressures (> 10 MPa).[11-14] These harsh operating conditions compound its high energy costs (consuming more than 1% of global energy), making the HB process unsustainable.[7,11,15-16] In addition, the HB process utilizes a supply of H_2 currently extracted largely from fossil fuels via reforming reactions, generating serious environmental problems[2] including huge greenhouse gas emissions.[17] Therefore, finding ways to produce ammonia electrochemically under mild operating conditions could contribute to a sustainable economy.

In nature, biological nitrogen fixation is an extremely important process, whereby microorganisms (such as azotobacter) use the enzyme nitrogenase, which catalyzes the reduction of N_2 to NH_3 under ambient conditions.[18] Such a process has motivated researchers to investigate numerous routes for artificial nitrogen fixation, including photocatalytic[19] and electrocatalytic[20] reduction of N_2, as well as bioelectrochemical methods.[21] The electrocatalytic nitrogen reduction

reaction (NRR) is an attractive route because it could be powered by excess renewable electricity and has the potential to reduce the required energy input, enabling sustainable ammonia synthesis.[12,22] The core concept in the electrocatalytic NRR is to identify efficient electrocatalysts[23-24] that can (1) reduce the reaction overpotential (i.e., provide a high ammonia yield rate near its thermodynamic equilibrium potential) and (2) increase ammonia formation selectivity (also known as Faradic efficiency, FE).[25-26] Although tremendous effort has been devoted to optimizing electrocatalysts for artificial nitrogen fixation,[27-32] candidates possessing the above two characteristics under ambient conditions remain elusive.

In recent years, heterogeneous electrocatalysts based on atomically dispersed transition metal (TM) atoms on a substrate have attracted attention and have been investigated extensively for diverse electrochemical reactions.[33-38] A single, adsorbed TM atom acts as a single-atom catalyst (SAC). Compared to their nanocluster counterparts, SACs not only minimize the amount of TM required but also may achieve high activity and selectivity due to the low-coordination environment of the isolated TM atoms.[39-43] As for the substrate, numerous novel two-dimensional (2D) materials, such as boron nitride,[44] nanoporous carbon,[45] graphene-based materials,[46] nitrogen-doped carbon,[47] graphdiyne,[48] TM dichalcogenides,[49] and graphitic carbon nitrides,[50-53] have been explored as potential electrocatalyst supports for the NRR.

By using a first-principles design approach, Hennig and co-workers predicted that single-layer III-V materials could be made.[54-55] A few years later, graphene-like 2D gallium nitride (g-GaN) was synthesized via a migration-enhanced encapsulated growth technique using epitaxial graphene.[56] Thereafter, free-standing GaN nanosheets were made by nitridation of metastable γ-Ga_2O_3[57] and the graphene-oxide-templating method.[58] As an analogue of graphene, the g-GaN monolayer opens up a new class of novel materials that could be used as substrates for NRR

electrocatalysts. Because GaN nanowires recently were found to exhibit improved N_2 photofixation activity with the aid of an ultra-small Ru cluster,[59] the question arises whether a single TM-atom-doped g-GaN monolayer (referred to as TM@g-GaN) can activate the inert N_2 molecule, and thereby provide a new route for artificial nitrogen fixation.

To address the above question, here we explore single TM atoms doped into the g-GaN monolayer as electrocatalysts for the NRR, by means of density functional theory (DFT) calculations. We predict that a Mo@g-GaN monolayer is optimal among the 15 TM-atom-doped g-GaN investigated here, as not only can it activate the inert N≡N triple bond but it also exhibits the highest NRR catalytic activity and highest selectivity toward ammonia synthesis. Mo@g-GaN achieves this via the so-called distal pathway (*vide infra*), with a low predicted onset potential of -0.33 V vs. the reversible hydrogen electrode (RHE). We therefore suggest that Mo@g-GaN be tested experimentally as a potential electrocatalyst for artificial nitrogen fixation.

2. COMPUTATIONAL DETAILS AND MODELS

Spin-polarized DFT calculations were performed using the Vienna *ab-initio* Simulation Package (VASP)[60-61] version 5.4.4 within the projector augmented-wave (PAW) formalism.[62-63] We used the generalized gradient approximation (GGA) of Perdew, Burke, and Ernzerhof (PBE)[64] for the DFT exchange-correlation (XC) functional. van der Waals interactions were described using the semi-empirical D3 correction method of Grimme et al.[65-66] We employed the standard VASP PAW PBE potentials for simulating the nuclei and frozen-core electrons of Ga, N, H, and the selected TMs (namely, Sc, Ti, V, Cr, Mn, Fe, Co, Ni, Cu, Zn, Mo, Ru, Rh, Pd, and Ag). The self-consistently calculated valence electrons were the $4s^2 4p^1$ for Ga, $2s^2 2p^3$ for N, $1s^1$ for H, $3d^1 4s^2$ for Sc, $3p^6 3d^2 4s^2$ for Ti, $3p^6 3d^3 4s^2$ for V, $3p^6 3d^5 4s^1$ for Cr, $3p^6 3d^5 4s^2$ for Mn, $3p^6 3d^6 4s^2$ for Fe,

105 $3p^6 3d^7 4s^2$ for Co, $3p^6 3d^8 4s^2$ for Ni, $3p^6 3d^{10} 4s^1$ for Cu, $3d^{10} 4s^2$ for Zn, $4d^5 5s^1$ for Mo, $4d^7 5s^1$ for
106 Ru, $4d^8 5s^1$ for Rh, $4d^{10}$ for Pd, and $4d^{10} 5s^1$ for Ag. We tested the sensitivity of the PAW potential
107 choice by trying three different potentials with different numbers of electrons solved for self-
108 consistently to predict the N_2 adsorption energy for the Mo-doped case. The predicted adsorption
109 energy variation is at most 0.08 eV while the relative adsorption energy (between end- and side-
110 on adsorption) variation is at most 0.01 eV (see Table S1 in the Supporting Information, SI), giving
111 the magnitude of the inherent uncertainty associated with the electron-ion representation.

112 To model the TM@g-GaN monolayer, we first structurally optimized the three-dimensional
113 wurtzite GaN primitive cell (space group $P6_3mc$) consisting of two basis atoms, using a 19×19×19
114 Γ-point-centered Monkhorst-Pack[67] k-point grid. The kinetic-energy cutoff for the plane-wave
115 basis was set to 500 eV. These parameters converged the total energy of a GaN primitive cell to
116 within 0.5 meV/atom (Figure S1 in the SI). The total energy and force thresholds for geometry
117 optimizations were respectively 1×10^{-5} eV and 0.03 eV/Å. Gaussian electronic smearing with a
118 width of 0.05 eV was used to aid electronic convergence for the bulk GaN and the undoped
119 monolayer. The resulting optimized lattice constants of bulk GaN are a=b=3.20 Å, c=5.21 Å,
120 α=β=90°, and γ=120°, in good agreement with experiment (a=b=3.19 Å, c=5.19 Å, α=β=90°, and
121 γ=120°).[68-69] We then built a 4×4 periodic monolayer supercell containing 16 Ga and 16 N atoms,
122 with a c-axis length for the simulation cell of 26 Å. This c-axis length provides at least 15 Å of
123 vacuum in the direction perpendicular to the monolayer plane when the adsorbates are added (*vide*
124 *infra*), which is sufficient to eliminate spurious interactions between periodic images. The
125 optimized GaN monolayer exhibits a graphene-like planar structure (g-GaN, see Figure S2 in the
126 SI), consistent with previous theoretical predictions.[54-55,70-77] We then substituted one Ga atom by
127 a single TM atom in the 4×4 supercell to generate each TM@g-GaN monolayer. The second-order

Methfessel-Paxton smearing method with a width of 0.1 eV was employed in the geometry optimizations for TM@g-GaN monolayers due to their metallic character. Dipole corrections along the surface normal were not taken into account because the implicit solvation model employed in this work (*vide infra*) already screens the surface dipole due to its dielectric response. The plane-averaged electrostatic potentials along the surface normal for the most polar structure, with and without dipole correction with potential correction, are shown in Figure S3 in the SI. It shows that the dipole correction leads to a non-convergent vacuum potential when employed together with the implicit solvation model. The optimized lattice constants of the TM@g-GaN monolayers deviate from those of the pristine g-GaN monolayer due to the stress introduced by the TM dopant (deviations are < 2%; see Table S2 in the SI). The fully optimized TM@g-GaN monolayer lattice vectors were used in subsequent calculations and were fixed during structural optimizations with adsorbates present. To examine whether the 4×4 supercell suffers from finite size effects, we performed calculations using a 5×5 supercell (using Mo@g-GaN as the test case). Adsorption energies of $^{*}N_2$, $^{*}NNH$, and $^{*}NH_2$ in the 4×4 and 5×5 supercells change by at most 0.02 eV/adsorbate (see Table S3 in the SI), indicating that the 4×4 supercell is large enough to simulate a dilute TM dopant concentration. The sampling of the Brillouin zone utilized a 5×5×1 Γ-point-centered Monkhorst-Pack k-point grid for geometry optimization and vibrational frequency calculations, while a denser 9×9×1 Γ-point-centered Monkhorst-Pack k-point grid was used for single-point energy calculations that converged the total energy to within 1 meV/formula-unit of GaN. Transition state (TS) geometries were identified using the climbing-image nudged elastic band (CI-NEB)[78] method within DFT-PBE-D3 with our mixed explicit-implicit solvation model described below. We interpolated nine images between the initial state (IS) and final state (FS) to determine the minimum energy path and the geometry of the TS. The TSs were verified through

151 frequency analysis that ensured only one imaginary frequency exists, assigned to be the minimum
152 energy path's unstable mode.

153 Although the pristine g-GaN monolayer is a semiconductor, most TM dopants give rise to
154 either *n*-type (Ti, V, Cr, Mn, Mo, Ru, and Rh) or *p*-type (Ni, Cu, Zn, Pd, and Ag) metallic character.
155 The rest, namely, Sc-, Fe(high-spin)-, and Co(high-spin)-doped g-GaN monolayers maintain an
156 electronic energy gap. Perhaps not surprisingly, those TMs that prefer oxidation states higher
157 (lower) than +3, i.e., the oxidation state of Ga in g-GaN, donate (accept) electrons to (from) g-
158 GaN. On the other hand, Sc, Co, and Fe, which can stably adopt a +3 oxidation state, act as neutral
159 defects. We employed DFT-PBE-D3 in order to obtain a fair comparison among the 15 TM atoms.
160 However, we also tested whether use of a Hubbard *U* correction would change the electronic
161 structure of the most promising candidate, namely, Mo@g-GaN (*vide infra*). We confirmed that it
162 exhibits *n-type* metallic character in both DFT-PBE-D3 and PBE+*U*-D3 theories[79-80] ($U_{eff} = U - J$
163 for the 4*d* orbitals of the Mo = 3.3 eV, derived from a constrained random phase approximation
164 calculation[81]). We therefore forgo the use of +*U* correction throughout, as the electron localization
165 this correction induces is unphysical for metallic systems.

166 Electron density changes upon N_2 adsorption on Mo@g-GaN were calculated as

167 $$\Delta\rho = \rho_{nH_2O-N_2-Mo@g-GaN} - \rho_{N_2} - \rho_{nH_2O-Mo@g-GaN},$$

168 where $\rho_{nH_2O-N_2-Mo@g-GaN}$ is the electron density of the Mo@g-GaN monolayer with *n* solvating
169 H_2O and adsorbed N_2, and ρ_{N_2} and $\rho_{nH_2O-Mo@g-GaN}$ are respectively the electron densities of the
170 isolated N_2 and the N_2-free Mo@g-GaN monolayer with *n* solvating water molecules (one for end-
171 on and two for side-on adsorbed N_2, *vide infra*), with geometries and atomic positions of the latter
172 two components taken directly from the composite structure. To investigate the chemical bonding

between the TM atom and the adsorbate, we conducted a projected crystal orbital Hamilton population (pCOHP) analysis,[82-84] as implemented in the LOBSTER code.[85]

A bulk-like water layer was not considered in this work due to the computational cost involved that would be prohibitive in this screening study. Instead, a mixed implicit + explicit solvation model was employed, where, in addition to the presence of an implicit solvation model[86-87] (i.e., a dielectric polarizable continuum solvation model with a dielectric constant of 78.4), explicit water molecules were included to hydrogen-bond with the adsorbates to mimic its immediate solvation environment. Such a mixed implicit + explicit solvation model was vetted and utilized previously while investigating CO_2 photoelectrochemical reduction,[88-90] and thus can be considered as a representative solvation environment for aqueous NRR as well. A detailed comparison between predictions derived using only an implicit solvation model vs. an implicit + explicit solvation model appears in Figure S4 of the SI. As seen there, the more sophisticated implicit + explicit solvation model not only changes the calculated Gibbs free energies in all cases but also alters the potential-determining step (PDS) in one case. We therefore employed the mixed implicit + explicit solvation model for the calculations of TM-atom screening for the TM@g-GaN monolayer (Section 3.1), N_2 adsorption on (Section 3.3) and electrocatalytic reduction of N_2 to ammonia on the Mo@g-GaN monolayer (Section 3.4), and for the kinetics of the most favored NRR pathway (Section 3.5). The implicit solvation model by itself was used for numerous test calculations, e.g., PAW potential selection (Table S1 in the SI), exploring structures of TM@g-GaN monolayers (Figure S2, Table S2 in the SI), supercell finite size error (Table S3 in the SI), first-principles molecular dynamics (FPMD) simulations of (Section 3.2, Figure S5 in the SI) and Mo atom diffusion on (Section 3.2, Figure S6 in the SI) the Mo@g-GaN monolayer, H adsorption on and

vacancy formation at lattice N sites (Section 3.2, Figure S7 in the SI), and surface oxidation (Section 3.2, Figure S7 in the SI).

In the initial screening to find suitable TM dopants, we introduced respectively one and two H_2O molecules for the end-on and side-on N_2 bonded to the TM dopants. This enables hydrogen bonding from an H atom in a solvating water molecule to the exposed lone pairs in $^*N_2$. Including two and three H_2O molecules respectively enables solvation of $^*NNH$ and $^*NNH_2$ via hydrogen bonds to the outer N atom lone pair (via an H atom in a water molecule) and to the H atom(s) of the adsorbates (via the O atom of a water molecule).

Six proton and electron transfer (PET) steps are involved in the NRR process ($N_2 + 6H^+ + 6e^- \rightarrow 2NH_3$). For each step, the proton and electron respectively transfer from the solution and the electrode to the adsorbate on the surface of the catalyst. The adsorption or reaction Gibbs free energy is defined as

$$\Delta G = \Delta E + \Delta ZPE + \Delta H - T\Delta S,$$

where ΔE is the adsorption or reaction internal energy change (taken here from 0 K DFT), ΔZPE is the change in the zero-point energy (ZPE), ΔH is the enthalpy change, T is temperature (here, room temperature, 298.15 K), and ΔS is the entropy change. The ZPEs and entropies of the adsorbed NRR species were computed from DFT vibrational frequencies; the vibrational modes of all atoms in the adsorbates and the TM@g-GaN monolayer were calculated explicitly at the Γ_{phonon} -point (full phonon dispersion was not considered; because the reactions are localized on the TM, we expect any phonon dispersion correction to be small). For all adsorbed intermediates on the TM@g-GaN monolayer, only the vibrational entropy needs to be taken into account because the translational and rotational degrees of freedom of the adsorbate effectively convert into

vibrational modes (frustrated translations and rotations). Enthalpies and entropies of the fluid-phase molecules, i.e., N_2(g), H_2(g), NH_3(g), and $H_2O(l)$, were obtained from the NIST database.[91]

We employed the computational hydrogen electrode (CHE) model proposed by Nørskov et al.[92] to establish the free energy profile for the electrochemical reduction reactions. In this model, the energy of a proton and electron pair ($H^+ + e^-$) is calculated conveniently as the energy of 1/2 H_2, as in the RHE.[93-94] Within the RHE, the chemical potential of a proton and electron pair is defined as

$$G(H^+ + e^-) = \frac{1}{2}G(H_2) - neU,$$

where n is the number of electrons involved in the reaction and U is the applied electrochemical potential relative to the RHE. In the case of the NRR investigated here, $n = 1$ for each elementary step. Therefore,

$$G(H^+ + e^-) = \frac{1}{2}G(H_2) - eU.$$

We compute the adsorption Gibbs free energies in the presence of m explicit water molecule(s) using the following equation:

$$\Delta G_{ads} = G(mH_2O + adsorbate + TM@g - GaN) - G(adsorbate) - G(mH_2O + TM@g - GaN),$$

where $G(mH_2O + adsorbate + TM@g - GaN)$, $G(adsorbate)$, and $G(mH_2O + TM@g - GaN)$ respectively are the Gibbs free energies of the solvated TM-doped GaN monolayer with the adsorbed species (i.e., $m$$H_2O$+adsorbate+TM@g-GaN), the isolated adsorbate in the gas phase (spin multiplicities of *NNH and $^*NH_2$ = 2; translational and rotational entropies computed using respectively the ideal gas and rigid-rotor models; vibrational entropy and integrated isobaric heat

capacity for these species calculated using DFT within the harmonic approximation), and the solvated TM@g-GaN monolayer containing only the explicit water molecule(s) (i.e., *m*H_2O+TM@g-GaN, where the relaxed water molecules are located roughly in the same positions as in the *m*H_2O+adsorbate+TM@g-GaN).

For other intermediates along the NRR pathway, the number of water molecules included in the calculations depends on the specific NRR mechanism under investigation. Specifically, we included five, seven, and four H_2O molecules respectively for the distal, alternating, and enzymatic pathways (*vide infra*). These numbers were determined by the minimum number of H_2O molecules needed to form hydrogen bonds with specific NRR intermediates along each pathway, namely, $^*N$ + NH_3, $^*NH_2$ + NH_3, and H_2N^*-$^*NH_2$ for the distal, alternating, and enzymatic pathways, respectively. The distances between the two N atoms in $^*N$ + NH_3 and $^*NH_2$ + NH_3 are both larger than 5 Å, where the NH_3 molecule is solvated with four explicit water molecules. These intermediates are the ones that require the highest number of solvating water molecules, based on the premise that every exposed lone pair will hydrogen-bond to an H in a water molecule and every H covalently bound to an N will hydrogen-bond to an O in a water molecule. With respect to the mixed NRR mechanisms, two additional H_2O molecules – compared to the five in the distal pathway – were added to the $^*NNH_2$ intermediate so that there would be the same number of water molecules (seven) for the reactant and product in either the isomerization between $^*NNH_2$ and $^*NHNH$ (in the mixed-A pathway, *vide infra*) or the protonation plus reduction reaction from $^*NNH_2$ to $^*NHNH_2$ (in the mixed-B pathway, *vide infra*).

Finally, whenever reaction free energies between reactants and products with different numbers of explicit water and/or NH_3 molecules were calculated (as in the case when different pathways cross where there is a common intermediate and when NH_3 is produced in the previous step and is

assumed to dissolve into bulk water), we add or subtract the free energy of a liquid water molecule and/or aqueous NH_3 accordingly to balance the reaction. The free energy of a water and NH_3 molecule in the liquid or solvated phase were determined from the energies and vibrational frequencies of an isolated implicitly solvated water or NH_3 molecule in a periodic box of 13.09 Å × 13.09 Å × 25.00 Å. On the other hand, in simulating desorption of the second NH_3 generated during the NRR process, this NH_3 instead was kept far away from the monolayer in the same supercell, together with four explicit solvating water molecules, just as was done for release of the first NH_3.

3. RESULTS AND DISCUSSION

3.1 Screening TM@g-GaN monolayers as NRR electrocatalysts

Nørskov and coworkers[22,95] proposed the following three screening criteria for NRR electrocatalysts. The catalyst must: (1) adsorb N_2, (2) stabilize $^*NNH$, and (3) destabilize $^*NH_2$. Here, 15 TM atoms (Sc, Ti, V, Cr, Mn, Fe, Co, Ni, Cu, Zn, Mo, Ru, Rh, Pd, and Ag) each were substituted for one Ga in the g-GaN monolayer as potential candidates. We calculated the adsorption Gibbs free energy of $^*N_2$ (both end-on and side-on configurations), $^*NNH$, and $^*NH_2$ on various TM@g-GaN monolayers (Figure 1a and Figure 1b), using the mixed implicit + explicit solvation model. Following criterion (1), we eliminated Sc, Ti, Cr, Mn, Fe, Co, Ni, Cu, Zn, Rh, Pd, and Ag due to their positive free energy of N_2 adsorption (Figure 1a). Following criteria (2) and (3), we subsequently excluded V and Ru because they both exhibit relatively weak stabilization of $^*NNH$ compared to Mo, while V also strongly binds $^*NH_2$ (Figure 1b). Further, we predict the Gibbs free energy change of the first protonation plus reduction process of the NRR to produce $^*NNH$ on the Ru@g-GaN monolayer to be 0.76 eV, which is 0.43 eV higher than the predicted

PDS of the NRR on the Mo@g-GaN monolayer (*vide infra*). This corresponds to an overpotential of 0.85 V vs. the RHE in the case of Ru, defined using the measured equilibrium potential for NRR of 0.09 V vs. the RHE.[96] The Mo@g-GaN monolayer thus is the only feasible NRR electrocatalyst among the TM dopants considered, as it satisfies all three screening criteria and therefore is the only one studied further here.

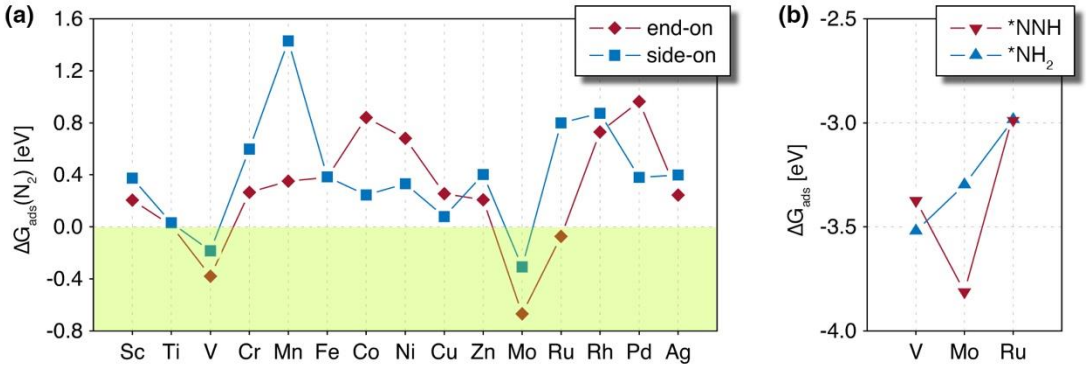

Figure 1. Adsorption Gibbs free energies for (a) $^{*}N_2$ and (b) $^{*}NNH$ and $^{*}NH_2$ on various TM@g-GaN monolayers, from DFT-PBE-D3 within a mixed implicit + explicit solvation model.

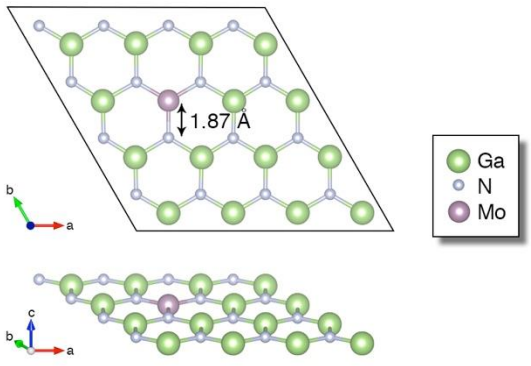

Figure 2. Top and side views of the 4×4 Mo@g-GaN monolayer's optimized geometry. One of the Mo-N bond lengths is annotated. All three Mo-N bonds are equal in length.

3.2 Structure and stability of the Mo@g-GaN monolayer

Figure 2 shows the optimized structure of the Mo@g-GaN monolayer. As shown in Table S4, the magnetization of the Mo atom in the Mo@g-GaN monolayer is 0 μ_B, which could correspond to either a Mo(IV) or Mo(VI) oxidation state. Despite its potential inaccuracy, qualitative trends in Bader charge analysis[97-99] can be instructive. Bader charge analysis shows the Mo is not fully oxidized, indicative then of a low-spin Mo^{4+}. The similar ionic radius of Mo^{4+} (65 pm) compared to Ga^{3+} (62 pm)[100] allows the Mo@g-GaN monolayer to retain the planar structure of the pristine g-GaN monolayer, with a Mo-N bond length (1.87 Å) only slightly larger than that of Ga-N (1.85 Å). Before proceeding further, we assess the stability of the Mo@g-GaN monolayer, because another requirement of a SAC is long-term stability.

We first assess the binding energy of Mo doped into g-GaN, because strong bonding between Mo and the anchoring material (the g-GaN monolayer with a Ga vacancy, referred to as V_{Ga}@g-GaN) is essential to prevent its degradation. The binding energy is defined as

$$\Delta G^{binding}_{Mo@g-GaN} = G_{Mo@g-GaN} - G_{V_{Ga}@g-GaN} - \mu_{Mo}.$$

According to the Pourbaix diagram of Mo,[101] Mo metal and Mo^{3+}(aq) are the two most stable phases at pH=0. The chemical potential of Mo therefore can be evaluated with respect to two references, Mo metal and Mo^{3+}(aq). Using Mo metal as the reference, the binding energy can be evaluated as

$$\Delta G^{binding,Mo\ metal}_{Mo@g-GaN} = G_{Mo@g-GaN} - G_{V_{Ga}@g-GaN} - G_{Mo,\mathrm{bcc}},$$

where $G_{Mo,bcc}$ is the Gibbs free energy of Mo in its ground-state body-centered cubic (bcc) crystal phase:

$$G_{Mo,bcc} = E_{Mo,bcc} + ZPE + H(0 \rightarrow 298.15K) - TS,$$

where $E_{Mo,bcc}$ is the electronic energy, ZPE is the zero-point energy, H is the isobaric enthalpy change from 0 K to 298.15 K, T is the temperature (298.15 K), and S is the entropy at 298.15 K. The last three terms were calculated from the full phonon spectrum of a two-atom Mo bcc supercell using the built-in Hessian and phonon frequency routine in VASP, where the electronic Brillouin zone was sampled using a 19×19×19 Γ-point-centered Monkhorst-Pack k-point grid for geometry optimization and vibrational frequency calculations, while a denser 23×23×23 Γ-point-centered Monkhorst-Pack k-point grid was used for calculation of the internal energy. From the above equations, $G_{Mo@g-GaN}^{binding,Mo\ metal}$ is predicted to be -6.40 eV. If instead we use Mo^{3+}(aq) as the reference, the binding energy can be expressed as

$$\Delta G_{Mo@g-GaN}^{binding,Mo^{3+}} = \Delta G_{Mo@g-GaN}^{binding,Mo\ metal} - \Delta G(Mo \rightarrow Mo^{3+}),$$

where

$$\Delta G(Mo \rightarrow Mo^{3+}) = \Delta G^{0}(Mo \rightarrow Mo^{3+}) + k_B T \ln[Mo^{3+}] - 3 \times U_{\text{vs. SHE}} \times |q|$$

is the Gibbs free energy change of the reaction $Mo(s) \rightleftarrows Mo^{3+} + 3e^{-}$ at potential $U_{\text{vs. SHE}}$ vs. the standard hydrogen electrode (SHE). Here, we use the experimental standard oxidation free energy of Mo(bcc) to Mo^{3+}(aq), which is $\Delta G^{0}(Mo \rightarrow Mo^{3+}) = -0.87$ eV *vs*. the SHE,[102] and where $|q|$ is the unit charge and $k_B T \ln[Mo^{3+}]$ is the concentration correction term. According to the experimental Pourbaix diagram,[101] Mo^{3+} is the stable phase when $U_{\text{vs. SHE}} > -0.4$ V vs. SHE (constructed with the concentration of Mo^{3+} equal to 1×10^{-6} M).[101] Thus, $G_{Mo@g-GaN}^{binding,Mo^{3+}} =$

$-6.40-(-0.87-3\times U_{\text{vs. SHE}}\times|q|)-k_BT\ln[Mo^{3+}]=-5.53+3\times U_{\text{vs.SHE}}\times|q|-k_BT\ln[Mo^{3+}]$ eV. The relevant NRR conditions are $0\le pH\le 7$ and $U_{\text{vs.RHE}}<0$ V. Thus, $G_{Mo@g-GaN}^{binding,Mo^{3+}}<-5.53$ eV at pH=0 and $[Mo^{3+}]$ = 1.0 M, indicating the strong binding between Mo atom and the anchoring material with a Ga vacancy.

We then examined the thermal stability of the Mo@g-GaN monolayer with respect to decomposition by performing implicitly solvated DFT-PBE-D3 FPMD simulations within the NVT ensemble at 300, 500, and 1000 K using the Nosé-Hoover scheme,[103-104] in which the time step was set to 1.0 fs for a total duration of 20 ps. As shown in Figure S5 of the SI, no notable reconstructions were observed after 20 ps at all three temperatures. The expense of such simulations forces us to assume that 20-ps-long trajectories are sufficient to represent the structure at longer times. Such a strategy was employed in previous investigations of 2D materials for electroreduction of N_2, with even shorter trajectories of 10 ps.[46,53,105-106]

We further assessed the stability of the Mo atom in the Mo@g-GaN monolayer by simulating the diffusion of a single Mo atom from the anchoring site to a neighboring hollow site.[44] The optimized geometries of the initial and final states and the Gibbs free energy profile of the diffusion process are shown in Figure S6. The Gibbs free energy change for this diffusion step is 7.18 eV, because of the formation of a cation vacancy and a Mo adatom. Mo thus will not diffuse out of the monolayer.

Next, we examined the protonation and reduction of the Mo@g-GaN monolayer via H adsorption onto N atoms within the lattice ($N^{latt.}$) and subsequent removal of the hydrogenated $N^{latt.}$. Catalyst decomposition via the formation of $N^{latt.}H_3$ would yield false activity for nitrogen reduction. As this is one of the persistent challenges in identifying viable NRR electrocatalysts, efforts have been made experimentally to ensure the detected ammonia is being generated from

nitrogen gas instead of from contamination or decomposition of the electrocatalyst itself.[107-111] We therefore investigated if the decomposition of the Mo@g-GaN monolayer through this path could take place or not, under the operating conditions of the electrocatalyst. We first examined the case of H adsorption on the $N^{latt.}$. Accordingly, we calculated the necessary first step toward $N^{latt.}H_3$ formation, namely adsorption of an H atom onto two chemically unique $N^{latt.}$ sites (see Figure S7a and Figure S7b) via DFT-PBE-D3 with implicit solvation. The two adsorption sites are a second-nearest-neighbor (labeled site A) and a nearest-neighbor (labeled site B) N of the Mo dopant. The H adsorption Gibbs free energies at these $N^{latt.}$ sites $\Delta G_{ads@N^{latt.}}(H)$ are predicted to be 0.98 and 0.81 eV at 0 V vs. the RHE for sites A and B, respectively. Later we show that the onset potential for the NRR is -0.33 V vs. the RHE on the Mo@g-GaN monolayer. At this potential, the $\Delta G_{ads@N^{latt.}}$(H)s would be respectively 0.65 and 0.48 eV for sites A and B. Thus, H adsorption on $N^{latt.}$ is relatively unfavorable thermodynamically compared to the NRR and a significantly more reducing potential, $\lesssim -1$ V, would be needed to initiate the hydrogenation of these sites. We then investigated if the decomposition of the substrate could take place by removing a $N^{latt.}$ atom to form NH_n, where n = 1, 2, and 3, leaving behind a N vacancy. We calculated these reactions via DFT-PBE-D3 with implicit solvation. As in the above, the N atom is taken from either sites A or B (Figure S7a) and the NH_n is moved above the surface (Figure S7c). We then computed the corresponding Gibbs free energy profile for these reactions (Figure S7d). The formation of NH exhibits the largest reaction Gibbs free energy change, namely, 6.16 and 6.24 eV at 0 V vs. the RHE for A- and B-sites, respectively. The free energy to form NH_3, although much lower than either NH_2 and NH formation, remains high: 1.94 and 1.71 eV at 0 V vs. the RHE for A- and B-sites, respectively, decreasing to 0.95 and 0.72 eV at -0.33 V vs. the RHE. Therefore, removing $N^{latt.}$ to form any NH_n species in solution is also unfavorable thermodynamically compared to the

NRR process (*vide infra*). Hence, decomposition of the Mo@g-GaN monolayer through this path is not expected to occur at NRR operating potentials, because the NRR itself will dominate.

Lastly, we examined the stability of the substrate (i.e., Mo@g-GaN monolayer) with respect to oxidation in the presence of O_2 and H_2O. Specifically, we investigated the formation of oxidized Mo and Ga sites where we add either two O, two OH, or one O and one OH, with one species on each side, or both on the same side of the Mo@g-GaN monolayer. We also considered mono- and bidentate O_2 adsorption. We found that for the Mo site, O=Mo=O@g-GaN, O=Mo-(OH)@g-GaN, and (OH)-Mo-(OH)@g-GaN configurations in which one adsorbate is above and one is below the monolayer are the most stable oxidation products. Figure S7e shows the optimized structures of these species, as well as the (much less stable) O_2 configurations. The formation of these oxidized species are described by the following reactions:

$$\text{Mo@g-GaN} + 2H_2O(l) \rightarrow \text{O=Mo=O@g-GaN} + 4(H^+ + e^-)$$

$$\text{Mo@g-GaN} + 2H_2O(l) \rightarrow \text{O=Mo-(OH)@g-GaN} + 3(H^+ + e^-)$$

$$\text{Mo@g-GaN} + 2H_2O(l) \rightarrow \text{(OH)-Mo-(OH)@g-GaN} + 2(H^+ + e^-)$$

in which the internal energy of $H_2O(l)$ was evaluated by means of the implicit solvation model solvating one water molecule; finite-temperature free-energy corrections were calculated from the computed vibrational Helmholtz free energy of the aforementioned solvated water molecule, along with the tabulated empirical enthalpy change from 0 K to 298 K and entropy at 298 K for liquid water (see COMPUTATIONAL DETAILS AND MODELS).

The above chemical equations avoid the explicit simulation of O_2 gas as an oxidant, a molecule that is over-bound within DFT-PBE by approximately 1 eV/O_2.[64] Moreover, these expressions enable the evaluation of the potential-dependent oxidation reaction free energies. Note that under

406 ambient and more oxidizing conditions, O_2 is the more likely oxidant, where the hydroxo species
407 are produced from the protonation of the oxo ligands. Under reducing potentials, O_2 is unstable
408 and H_2O thus becomes the primary oxidant (which is itself reduced), producing H_2 as its reduction
409 product. Thus, another advantage of the above expressions is their independence from the identity
410 of the oxidant, where the oxidizing power of the environment is instead tuned via the applied
411 potential in the Nernstian fashion (Supplementary Note 1 in the SI). At 0 V vs. the RHE, the
412 oxidation Gibbs free energies are predicted to be −0.08, −1.29, and −1.16 eV for the formation
413 of O=Mo=O@g-GaN, O=Mo-(OH)@g-GaN, and (OH)-Mo-(OH)@g-GaN, respectively. On the
414 other hand, at the NRR onset potential of −0.33 V vs. the RHE (*vide infra*) on the Mo@g-GaN
415 monolayer, the oxidation Gibbs free energy of these three reactions become +1.24, −0.30, and
416 −0.50 eV. Later, we show that the adsorption of N_2 via the end-on configuration features an
417 adsorption Gibbs free energy of −0.67 eV. Therefore, end-on N_2 adsorption (i.e., the first step of
418 the NRR) should dominate over the formation of these oxidation products on the Mo site at the
419 NRR onset potential.

420 We performed similar calculations on a Ga site nearest to Mo, where we add only an O, OH,
421 or O_2 on one side, since we expect Ga^{3+} to be more resistant to further oxidation compared to Mo^{4+}.
422 We found that Ga=O on Mo@g-GaN is not stable, as the O atom spontaneously diffuses to the
423 adjacent Mo atom (forming Mo=O@g-GaN) during geometry optimization (Figure S7e). The
424 predicted reaction Gibbs free energies are −1.28, −0.47, and +2.98 eV at 0 V vs. the RHE for the
425 formation of Mo=O, Ga-OH, and Ga-O_2, respectively, which become −0.62, −0.14, and +4.30 eV
426 at the onset potential of −0.33 V vs. the RHE. N_2 adsorption via the end-on configuration thus has
427 a similar driving force to the formation of Mo=O@g-GaN at the NRR onset potential. The slightly
428 spontaneous formation of Ga-OH is likely due to the excess electron introduced by Mo into the

host g-GaN (*vide supra*), since it prefers an oxidation state of +4 over +3. Indeed, the addition of OH on pristine g-GaN (forming Ga-OH) we predict to be highly non-spontaneous (+1.58 eV at 0 V vs. the RHE, +1.91 eV at −0.33 V vs. the RHE). Encouragingly, the adsorption of N_2 on the Mo site (which draws a full electron to itself, *vide infra*) suppresses the formation of Ga-OH on Mo@g-GaN (0.00 eV at 0 V vs. the RHE, +0.33 eV at −0.33 V vs. the RHE). Moreover, we find that water does not adsorb (positive adsorption free energies, see the SI) onto either Ga or Mo sites, suggesting that water may not easily act as an oxidant (the most likely oxidant under reducing conditions). Taken altogether, these results indicate that the Mo@g-GaN monolayer should be stable against oxidation of the Mo and Ga sites when in the presence of N_2 and at the NRR onset potential. The results suggest that the proposed electrocatalyst (Mo@g-GaN) may need to be prepared in a glove box under nitrogen, otherwise initial oxidation could take place. On the other hand, under the reducing conditions of the electrocatalysis and in the presence of nitrogen, the catalyst may eliminate any oxide during operation.

To conclude, the large negative binding energy of the dopant Mo, probable thermal stability, large kinetic and thermodynamic stability of the Mo atom with respect to egress and diffusion, the relatively unfavorable hydrogenation of the $N^{latt.}$ sites and their eventual removal as NH_x, and the stability of the substrate against oxidation in the presence of nitrogen, suggest sufficient overall stability of the Mo@g-GaN monolayer and attest to the likely robustness of this potential electrocatalyst.

3.3 Adsorption of N_2 on the Mo@g-GaN monolayer

Chemisorption of N_2 onto the catalyst is a prerequisite for subsequent efficient NRR catalysis.[44,46] Both occupied and unoccupied TM *d*-orbitals participate in N_2 chemisorption and

activation of the inert N≡N triple bond via well-known donor-acceptor interactions. Unoccupied *d*-orbitals on the TM atom can accept lone-pair or π electron donation from N_2. Meanwhile, occupied TM *d*-orbitals can back-donate electrons to the anti-bonding π^* orbitals of N_2, which weakens the N≡N triple bond.

The optimized structures of the N_2-Mo@g-GaN monolayer with end-on and side-on N_2 configurations are shown in Figure 3a and Figure 3b, respectively. After adsorption of N_2, the Mo atom moves out of plane slightly compared to the bare Mo@g-GaN monolayer. The adsorption energies are -1.25 and -0.84 eV for the end-on and side-on configurations, respectively. After inclusion of ZPE and thermal corrections, the adsorption Gibbs free energies are -0.67 and -0.31 eV for the end-on and side-on motifs, respectively. Thus, adsorption of N_2 on the Mo@g-GaN monolayer via both end-on and side-on configurations are energetically favorable.

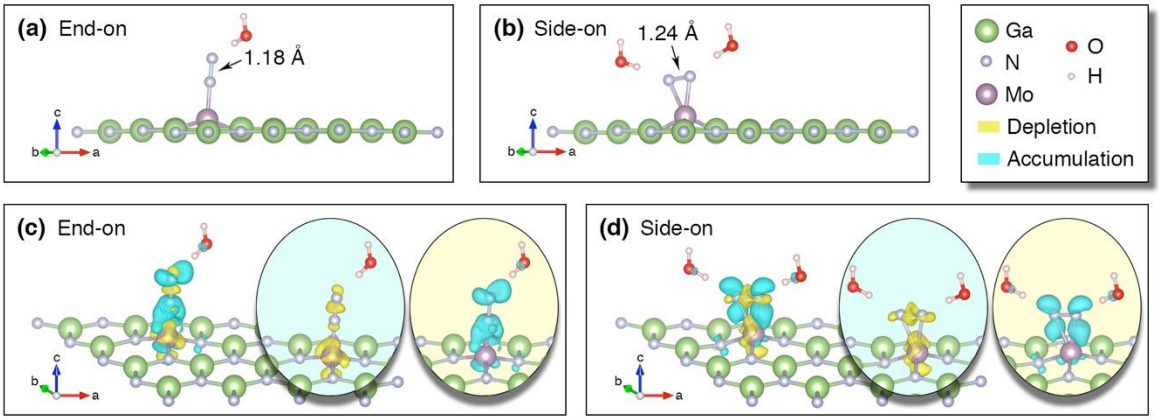

Figure 3. Side views of the optimized geometries of N_2-Mo@g-GaN in the (a) end-on and (b) side-on configurations, as predicted by DFT-PBE-D3 with a mixed implicit + explicit solvation model. Electron density changes in Mo@g-GaN upon adsorption of N_2 via (c) end-on and (d) side-on motifs. The isosurface value is 0.008 e/Å^3, where yellow and cyan isosurfaces indicate electron

density depletion and accumulation, respectively. The insets separately show the electron density depletion (yellow isosurface with cyan background) and accumulation (cyan isosurface with yellow background).

The N-N bond length elongates to 1.18 and 1.24 Å for the end-on and side-on configurations (Figure 3a and Figure 3b), respectively, compared to 1.098 Å in a gas-phase N_2 molecule. Bader charge analysis suggests that the two N atoms together gain approximately one electron in either configuration [0.79 *e* + 0.19 *e* (0.98 *e* in total) for end-on and 0.56 *e* + 0.50 *e* (1.06 *e* in total) for side-on] from the Mo@g-GaN monolayer. These values are much larger than the 0.29 *e* total electron transfer predicted by DFT-PBE for N_2 adsorption on a Mo-doped hexagonal boron nitride (Mo@*h*-BN) monolayer.[44] This suggests that the Mo@g-GaN monolayer is a better electron donor than the previously studied NRR catalyst Mo@*h*-BN monolayer. These trends also suggest that the inert N≡N triple bond might be more activated on the Mo@g-GaN monolayer.

Electron density difference isosurfaces for N_2 adsorption on Mo@g-GaN appear in Figures 3c and 3d for end-on and side-on configurations, respectively. More often than not, charge transfer is one-way from one species to another, depending on their relative electron accepting and donating ability. However, charge transfer here is bidirectional in that charge accumulation and depletion occurs for both the adsorbed N_2 and Mo atom. Such an observation is in accord with the donor-acceptor bonding mechanism mentioned earlier.

Despite the prediction that adsorption of N_2 on the Mo@g-GaN monolayer via end-on (adsorption Gibbs free energy -0.67 eV) is more favorable than side-on (adsorption Gibbs free energy -0.31 eV), the latter exhibits a longer N-N bond and more charge transfer, as discussed above. To understand this behavior, we performed a pCOHP analysis to examine the interaction

between the Mo atom and the nearest N atom in adsorbed N_2. The pCOHP analysis of end-on and side-on configurations for the spin-up component (similar results for the spin-down component are shown in Figure S8 in the SI) is displayed in Figure 4 as the negative of the pCOHP so that the populations above and below zero on the horizontal axis (depicted respectively by the red and blue shaded regions) indicate bonding and anti-bonding contributions, respectively. For the end-on configuration, all valence bands (below the Fermi level, E_F, which is set to zero) appear as bonding Mo-N orbitals, while all Mo-N anti-bonding orbitals are located above E_F (Figure 4a), consistent with the exoergic adsorption of N_2 on the Mo@g-GaN monolayer in this geometry. By contrast, in the side-on configuration (Figure 4b), the Mo-N_2 anti-bonding orbitals population increases. This manifests as a decrease in the negative of the integrated COHP (-ICOHP) going from end-on to side-on bonding (beneath each plot in Figure 4). -ICOHP is the difference in the total occupation of the bonding and anti-bonding Mo-N states, which therefore serve as a measure of their relative Mo-N bond strength. Furthermore, the separation between bonding and anti-bonding states near the Fermi level is much smaller in the side-on structure than in the end-on case. The above-mentioned trends are consistent with the less negative adsorption Gibbs free energy for the side-on adsorbed N_2.

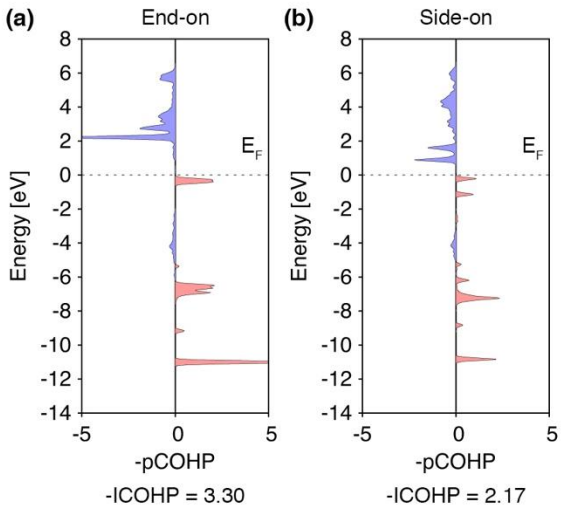

508

509 **Figure 4.** pCOHP analysis between the Mo atom and the nearest N atom in N_2 adsorbed via the
510 (a) end-on and (b) side-on configurations on the Mo@g-GaN monolayer, for the spin-up
511 component (see Figure S8 for the spin-down component), based on DFT-PBE-D3 calculations with
512 a mixed implicit + explicit solvation model. The Fermi level (E_F) is set to the reference energy of
513 0 eV in the pCOHP analysis. Red and blue shaded regions denote bonding and anti-bonding
514 contributions, respectively. The negative of the integrated COHP (-ICOHP) values are presented
515 under each panel.

516

517 3.4 Electrocatalytic reduction of N_2 into ammonia on the Mo@g-GaN monolayer

518 We briefly considered activation of N_2 via direct dissociation into two adsorbed N atoms on
519 the Mo@g-GaN monolayer. Such dissociation from the side-on adsorbed N_2 configuration using
520 only implicit solvation (see Figure S9 in the SI) incurs a minimum endoergicity of 1.73 eV,
521 indicating that such dissociation is unfavorable and therefore is not considered further. Instead,
522 activation of N_2 must involve hydrogenation via one or more associative mechanisms discussed
523 next.

We therefore investigated the NRR elementary steps of three possible associative mechanisms, namely, distal, alternating, and enzymatic, as depicted schematically in Figure 5a. In the associative mechanisms, step 1 involves the adsorption of N_2 on the Mo@g-GaN monolayer's surface, with protonation and reduction processes comprising steps 2-7. Figures 5b-d show the optimized geometries of each NRR intermediate (with the mixed implicit + explicit solvation model) for each elementary step on the Mo@g-GaN monolayer, via the distal, alternating, and enzymatic mechanisms, respectively, while Figures 6a-c display the corresponding predicted Gibbs free energy diagrams for these pathways.

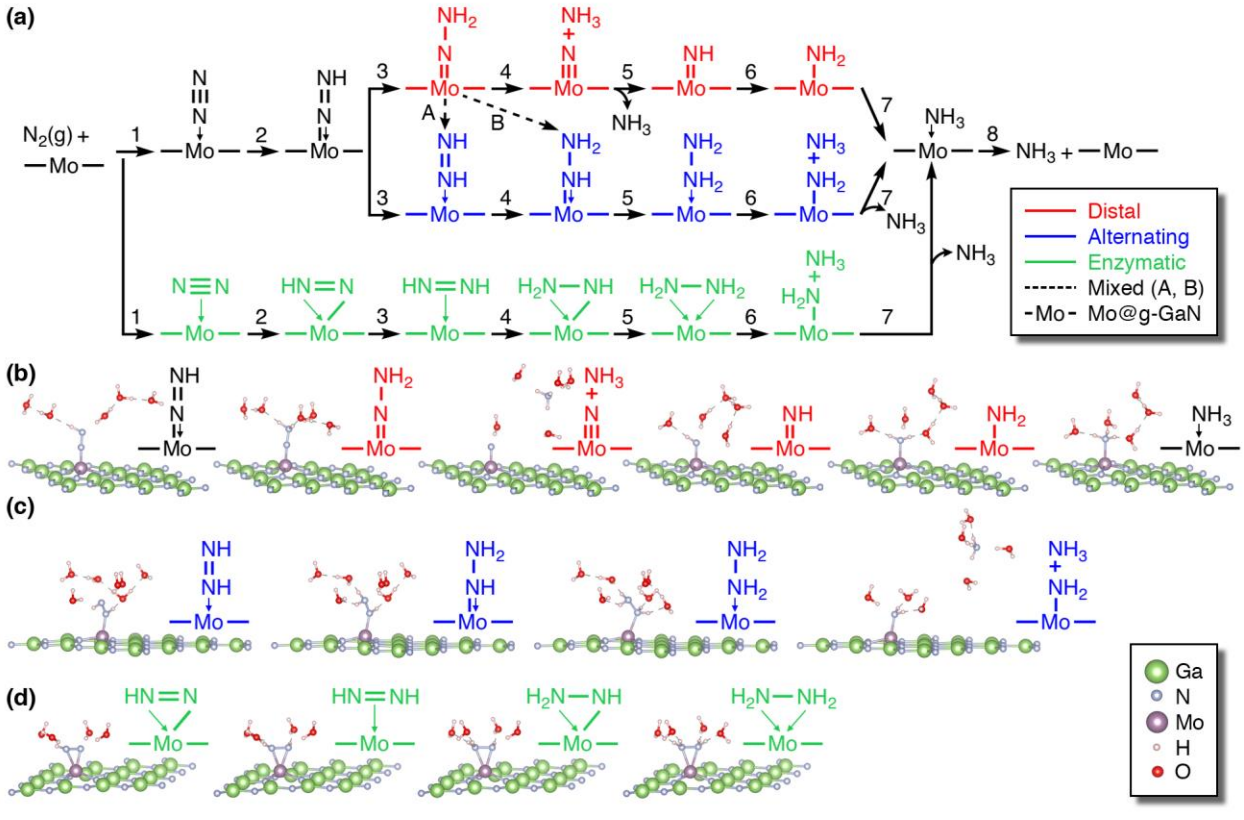

Figure 5. (a) Schematics of three possible associative mechanisms for N_2 electroreduction to NH_3 on the Mo@g-GaN monolayer. Optimized geometries of all possible intermediates along the NRR

pathway on the Mo@g-GaN monolayer through (b) distal, (c) alternating, and (d) enzymatic mechanisms using DFT-PBE-D3 with a mixed implicit + explicit solvation model. Each step 2-7 involves addition of a proton and an electron. Arrows and solid lines in the chemical formulas represent dative and covalent bonds, respectively.

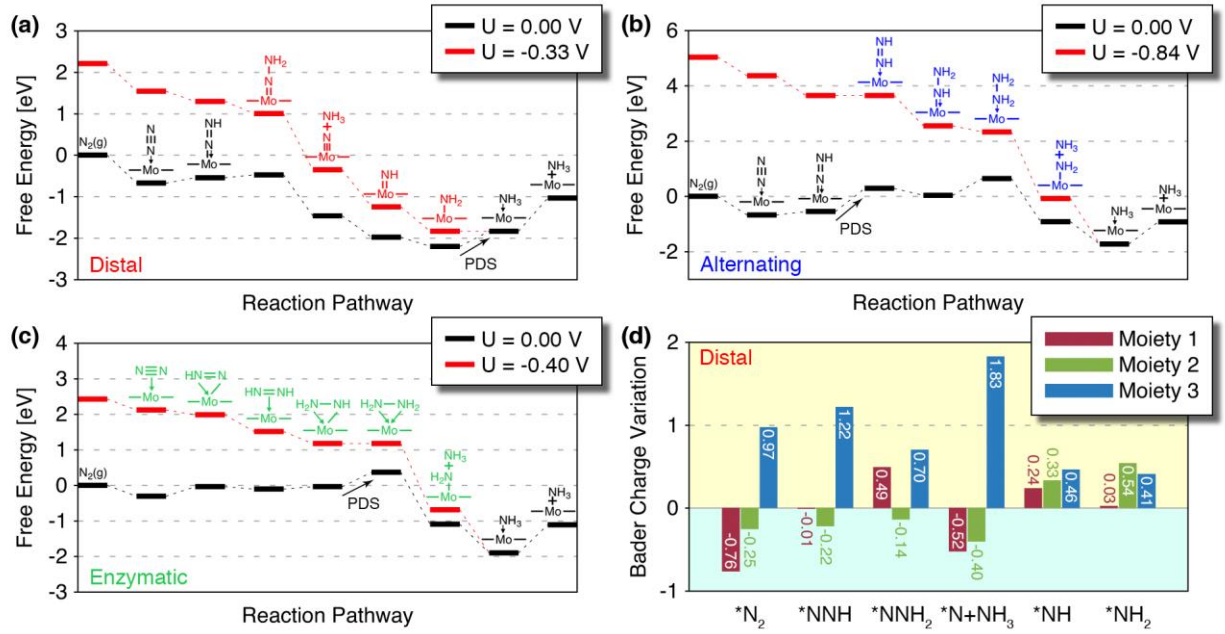

Figure 6. Gibbs free energy diagrams for the NRR on the Mo@g-GaN monolayer at zero and applied potentials equal to their respective onset potentials, via (a) distal, (b) alternating, and (c) enzymatic mechanisms, using DFT-PBE-D3 with a mixed implicit + explicit solvation model. The PDS is labeled in each Gibbs free energy diagram. Note the change in vertical scale in (a) vs. (b) and (c). (d) Bader charge variation of the three moieties along the distal pathway. Moieties 1, 2, and 3 are the g-GaN monolayer, the Mo atom and its three nearest-neighbor N atoms, and the adsorbed species N_xH_y. Yellow (positive values) and light blue (negative values) regions represent gained loss of electrons, respectively.

When the NRR follows the distal pathway, the adsorbed end-on $^{*}N_2$ will fully hydrogenate the outermost N atom first, by accepting a sequence of proton and electron pairs, first leading to the formation of $^{*}NNH$ on the Mo atom (see Figures 5a and b). After the first protonation plus reduction step (step 2 in Figure 5a), the N-N bond length elongates from 1.18 Å to 1.28 Å. This elementary step is slightly uphill energetically, with a reaction Gibbs free energy of 0.12 eV (Figure 6a). The second protonation plus reduction step then forms $^{*}NNH_2$, with a smaller reaction Gibbs free energy of 0.08 eV, where the N-N bond further stretches to 1.35 Å (step 3). The first NH_3 molecule is released from the Mo@g-GaN monolayer after the third protonation plus reduction (step 4), solvated by four water molecules, leaving one N atom on top of the Mo atom. This first NH_3-releasing step is highly exoergic, with a reaction Gibbs free energy of -0.99 eV (Figure 6a), driven by the formation of a Mo-N triple bond. Subsequently, the remaining adsorbed $^{*}N$ will go through three individual protonation plus reduction steps by reacting with one proton and one electron three times, resulting in the nonelectroactive release of the second NH_3 molecule (last four steps for the distal pathway in Figure 5a). The reaction Gibbs free energies for these four elementary steps are -0.52, -0.22, 0.33, and 0.79 eV, respectively (last four steps in Figure 6a). Note that after step 5, the first NH_3 molecule, generated in step 4, remains solvated in our model along the entire pathway. To retain a consistent number of explicit water molecules along the reaction pathways while keeping the first released NH_3 in solution, we carry along the energy of an implicitly solvated NH_3 in the subsequent steps. The desorption of the second NH_3 (step 8), consistent with what was modeled in step 4 for the first NH_3 release, was simulated by moving the NH_3 far away from the monolayer together with four out of the five explicit water molecules solvating it. The two solvated NH_3 molecules generated then may be protonated further to NH_4^+ in the solution, depending on the pH. The energy of this process is not calculated because it is not

574 a PDS and it is exoergic under acidic conditions. Such a calculation also would require further
575 examination of the proper solvation and charge compensation methods to be performed
576 accurately.[95,112] Concerted desorption and protonation of NH_3 should make the nonelectroactive
577 step 8 less endoergic, given that the experimental standard reaction free energy for the protonation
578 of NH_3(aq) to NH_4^+(aq) is -0.55 eV.[96] The last protonation plus reduction step (step 7 in Figure 5a,
579 involving the last two structures in Figure 5b) converting $^*NH_2$ to $^*NH_3$ is predicted to be the PDS
580 in the distal pathway, having the maximum ΔG (0.33 eV) among all electroactive elementary steps
581 (Figure 6a).

582 In both of the other pathways, namely, alternating (blue path) and enzymatic (green path),
583 shown in Figure 5a, the two N atoms are hydrogenated in turns. The difference between the two
584 pathways is that in the former the N_2 and the N_2H_x intermediates are bound end-on to Mo, while
585 in the latter, these species are bound side-on to Mo. In what follows, we discuss the alternating
586 path; however, the intermediates of both the alternating and enzymatic pathways share the same
587 basic structural features, the difference being only in the orientations of the bound N_2 and N_2H_x.
588 The alternating nature of adding H on the bound N_2 in the alternating pathway yields relatively
589 stable molecular hydrogenated dinitrogen species (relative to the intermediates of the distal
590 pathway), namely, diazene, N_2H_2 (after step 3) and hydrazine, N_2H_4 (after step 5). These closed-
591 shell molecular species thus are bound to Mo via dative bonding, where the molecules donate an
592 electron pair into empty Mo 4*d* states. Only at the fifth hydrogenation step (step 6) is the first
593 ammonia produced (NH_2 + NH_3), where the NH_3 molecule desorbs into the solution (Figure 5c).
594 The appearance of the closed-shell species as intermediates (N_2H_2 and N_2H_4) support the inclusion
595 of these two pathways as prime candidates for electrochemical ammonia synthesis. However,
596 based on the free energies of their respective PDSs, neither pathway is more favorable than the

distal pathway. In addition, after step 7 in both of these pathways, the first NH_3 molecule, which was generated in step 6, remains solvated, where an isolated NH_3 molecule (in another separate box, *vide supra*) that is implicitly solvated is simulated as in the distal pathway. Therefore, this molecule is no longer explicitly modeled together with the substrate and $^*NH_3$ in the product of step 7. The PDSs in the alternating and enzymatic mechanisms are the second (formation of diazene) and fourth (formation of hydrazine) protonation plus reduction steps (i.e., step 3 and 5 in Figure 5a, shown in blue and green), respectively. The reaction Gibbs free energy for each NRR elementary step in the alternating and enzymatic mechanisms are shown in more detail in Figures S4b and Figures S4c of the SI. The weakened interaction of these closed-shell intermediates with Mo appear to make these pathways unfavorable. Without any applied electrode potential, the endoergicity of 0.33 eV required for the protonation plus one-electron reduction of $^*NH_2$ to form $^*NH_3$ in the distal pathway is lower than those of the alternating (0.84 eV, Figure 6b) and enzymatic (0.40 eV, Figure 6c) mechanisms, suggesting a preference for the distal mechanism. Note that given an expected modeling error of ~0.1 eV, the enzymatic pathway also could be a viable mechanism (required potential is -0.40 V vs. -0.33 V for the distal pathway). However, end-on attachment of N_2 is more favorable than side-on by -0.36 eV (*vide supra*). Therefore, although the enzymatic pathway may contribute, the distal pathway is expected to dominate the NRR kinetics on the Mo@g-GaN monolayer.

In electrocatalysis, the onset potential and overpotential η are two commonly used descriptors of catalytic reactivity, where a less negative onset potential and a small overpotential value implies a faster process at a given potential. We therefore calculated onset potentials and thermodynamic overpotentials for the NRR on the Mo@g-GaN monolayer for these three mechanisms. According to the CHE,[92] the theoretical overpotential can be determined via

$$\eta = U_{equilibrium} - U_{PDS},$$

where $U_{equilibrium}$ is the equilibrium potential of the NRR and U_{PDS} is the minimum potential required to make the PDS spontaneous (the latter defines the onset potential). The $U_{equilibrium}$ used for the NRR reaction $N_2(g) + 6H^+ + 6e^- \rightarrow 2NH_3(aq)$ is +0.09 V vs. the RHE, which is taken from tabulated experimental standard reduction potentials.[96] Our theoretical prediction (i.e., +0.17 V vs. the RHE) is consistent with this experimental value. U_{PDS} (in V) is expressed as

$$U_{PDS} = -\Delta G_{PDS}/e,$$

where ΔG_{PDS} is the Gibbs free energy change of the PDS (in eV), and e is the electron charge (= 1). Thus, the U_{PDS} for the distal, alternating, and enzymatic pathways are -0.33, -0.84, and -0.40 V, respectively. The overpotentials η for the distal, alternating, and enzymatic mechanisms thus are $(0.09\ \text{V}) - (-0.33\ \text{V}) = 0.42\ \text{V}$, $(0.09\ \text{V}) - (-0.84\ \text{V}) = 0.93\ \text{V}$, and $(0.09\ \text{V}) - (-0.40\ \text{V}) = 0.49\ \text{V}$, respectively. Thus, we predict that the NRR will proceed on the Mo@g-GaN monolayer via the distal pathway, due to its less negative onset potential of -0.33 V vs. the RHE and the smallest corresponding overpotential of 0.42 V vs. the RHE, via the more favorable end-on bonding of N_2 on Mo (*vide supra*). Such an onset potential is substantially less negative than those predicted for well-established electrochemical NH_3-synthesis catalysts such as Re(111) (-1.1 V vs. the RHE)[22] and rocksalt ZrN(100) (-0.76 V vs. the RHE) surfaces.[113] The Mo@g-GaN monolayer therefore is a promising electrocatalyst for the NRR process.

We also examined two recently proposed mixed NRR pathways,[28,114-116] in which the $^*NNH_2$ species in the distal mechanism transitions to the alternating pathway, either to form, via isomerization, $^*NHNH$ (dashed arrow A after step 3 in Figure 5a) or, via further protonation/reduction, $^*NHNH_2$ (dashed arrow B after step 3 in Figure 5a). Figure S10 in the SI

displays the resulting predicted Gibbs free energy diagrams for the mixed-A and mixed-B mechanisms. We predict that the PDS remains the fourth protonation plus reduction step for both mixed mechanisms, namely, the protonation/reduction of $^{*}NHNH_2$ to $^{*}NH_2NH_2$ with an endoergicity of 0.61 eV. This value is higher than the 0.33 eV predicted in the pure distal mechanism. Moreover, even at an applied potential of −0.61 V vs. the RHE, an uphill, potential-independent step exists with a Gibbs free energy change of 0.58 eV in the mixed-A pathway (labeled as ΔG_r in Figure S10a), associated with isomerization of $^{*}NNH_2$ to $^{*}NHNH$. The mixed mechanisms therefore are less favorable energetically than the distal pathway.

Variations in the configurations of the explicit water molecules employed in our calculations could affect the computed Gibbs free energy profiles. We therefore considered a second set of configurations for the explicit water molecules solvating the NRR intermediates along the distal pathway, to estimate the magnitude of this effect. In the second set of water structures, we moved the second-shell water molecules (those not directly in contact with the adsorbates), while we kept the same first-shell water structures, and subsequently re-optimized the full structures. The second-shell water molecules were moved such that different first-shell water molecules were solvated explicitly or the shape of the solvating water clusters was modified. The magnitude of the displacements were ~ 2 to 4 Å. Optimized geometries of the NRR intermediates and predicted reaction Gibbs free energies for the second set of water configurations are shown in Figure S11a and Figure S11b, respectively. As shown in Figure S11b, employing alternative water configurations does not change the identity of the PDS (step 7). Moreover, the predicted reaction Gibbs free energy of the PDS changed only by 0.02 eV. Therefore, the effect of varying water configurations on the predicted PDS and reaction Gibbs free energy is expected to be negligible, provided the first solvation shell is included appropriately as done here.

To understand the origins of these reactivity trends for the NRR on the Mo@g-GaN monolayer, we evaluated the Bader charge change after each protonation/reduction step in the most favorable distal pathway (Figure 6d). Following similar analysis conducted on other NRR catalysts,[44,46] we deconstruct N_xH_y-Mo@g-GaN into the following parts: moiety 1 (the g-GaN monolayer without moiety 2 atoms), moiety 2 (Mo and its nearest-neighbor lattice N atoms, i.e., Mo-N_3), and moiety 3 (the adsorbed species, not including the solvating water molecules). For step 1: Upon adsorption of end-on N_2 on the Mo@g-GaN monolayer, N_2 gains 0.97 electrons, where the substrate and Mo-N_3 contribute about 75% and 25% of the transferred charge, respectively. The overall net charge change is 0 because this step does not involve PET. Step 2 of $^*N_2 \rightarrow {}^*NNH$: $^*NNH$ gains 1.22 electrons, in which 0.01/0.22/0.99 (i.e., 1.22-0.01-0.22) electrons respectively come from the substrate/Mo-N_3/($H^+ + e^-$). Step 3 of $^*NNH \rightarrow {}^*NNH_2$: $^*NNH_2$ and substrate respectively gain 0.70 and 0.49 electrons, where Mo-N_3/($H^+ + e^-$) respectively contribute 0.14/1.05 (i.e., 0.70+0.49-0.14) electrons. Step 4 of $^*NNH_2 \rightarrow {}^*N + NH_3$: $^*N + NH_3$ gains 1.83 electrons in total ($^*N$ and NH_3 respectively gain 0.67 and 1.16 electrons), with 0.52/0.40 electrons coming from the substrate/Mo-N_3 and the remaining 0.91 (i.e., 1.83-0.52-0.40) electrons originating from the ($H^+ + e^-$). Step 5 of $^*N + NH_3 \rightarrow {}^*NH + NH_{3(aq)}$: $^*NH$, Mo-N_3, and the substrate respectively gain 0.46, 0.33, and 0.24 electrons from the ($H^+ + e^-$). Step 6 of $^*NH \rightarrow {}^*NH_2$: $^*NH_2$, Mo-N_3, and the substrate respectively gain 0.41, 0.54, and 0.03 electrons from the ($H^+ + e^-$).

From step 2 to step 6, the net electron change in each step is ~1 because each step involves a PET process. These numbers do not add up to unity in our discussion above because of numerical uncertainty introduced in the integration of the Bader charges. Based on our above analysis, moiety 1 acts as the primary electron donor or acceptor during the NRR pathway, i.e., as an electron

687 reservoir, while moiety 2 is the active site for the reduction of N_2 and thus mediates the electron
688 transfer between the substrate and adsorbates, although it also acts an electron sink and source.
689
690 3.5 Kinetics of the NRR via the favored distal pathway
691 While the thermodynamic analyses presented so far are fairly compelling, it is important to
692 verify there will be no large kinetic barriers to the NRR through its most thermodynamically
693 favored route. This section thus presents an assessment of the activation free energies of the two
694 key elementary steps in the NRR through the favored distal pathway. We use the same
695 computational set up as with our evaluation of the NRR thermodynamics. We consider the initial
696 activation of N_2 via its adsorption in the end-on configuration and the PDS (step 7 in Figure 5a)
697 converting $^*NH_2$ to $^*NH_3$, which involves the transfer of an electron and a proton, because the
698 latter is the least thermodynamically favored step (0.33 eV endoergic at 0 V vs. the RHE) and
699 therefore likely to have the highest barrier.
700 The geometries of the initial state (IS), transition state (TS), and final state (FS) for the N_2
701 adsorption step are shown in Figure 7a, with a calculated activation free energy of 0.14 eV. Note
702 that the free energy of reaction and barrier of this step is potential-independent. Furthermore, this
703 small activation barrier is easily surmountable at room temperature, so initial activation of N_2 via
704 end-on adsorption will readily occur.
705 As for the PDS (a potential-dependent step) converting $^*NH_2$ to $^*NH_3$, we included an
706 additional explicit H_2O molecule and one H_3O molecule to form an Eigen cation (Figure 7b). The
707 H_3O molecule spontaneously ionizes into H_3O^+, with the substrate acquiring a net negative charge
708 (with an excess of 0.848 electrons, see Table S4). By including an explicit Eigen cation, we can
709 simulate directly the transfer of one proton (from water adjacent to H_3O^+, with the latter

transferring its excess proton to the deprotonated water in a shuttle mechanism) and one electron to the adsorbate ($^{*}NH_2$). The optimized geometries of the stationary and transition-state structures for this step appear in Figure 7b. We then determined the linear relationships between the reaction/activation Gibbs free energy ($\Delta G_r/\Delta G^{\ddagger}$) and the (relative) work function and absolute charge state of the catalyst, $\Delta\Phi$, following the method proposed by Chan and Norskøv[117-118] (blue and red dashed lines in Figure 7c). The method enables the determination of ΔG_r and $\Delta G^{\ddagger}$ at constant potential from constant charge simulations. Here $\Delta\Phi$ is defined as the work function of the Mo@g-GaN layer relative to the energy level of the implicit solvation model representing bulk water (see Supplementary Note 2 in the SI). To determine $\Delta G^{\ddagger}$ at 0 V vs. the RHE, we first locate the corresponding $\Delta\Phi$ for ΔG_r= 0.33 eV (i.e., the reaction Gibbs free energy of the PDS, step 7, from the CHE model) – point A in Figure 7c. $\Delta G^{\ddagger}$ at 0 V vs. the RHE (point B) is thus the Gibbs free energy of activation of the PDS at the same $\Delta\Phi$ as point A, which is 0.49 eV. Next we identify the value of $\Delta\Phi$ for which ΔG_r= 0 eV – point C in Figure 7c. The corresponding shift along $\Delta\Phi$ is -0.41 eV, which is a 0.08 V more negative onset potential than the CHE model prediction of -0.33 V vs. the RHE. We then identify $\Delta G^{\ddagger}$ at this new onset potential (same $\Delta\Phi$ as point C, but along the $\Delta G^{\ddagger}$ line) to be 0.42 eV (point D). Therefore, the proposed electrocatalyst Mo@g-GaN not only has a low onset potential of -0.33 V vs. the RHE, but also exhibits readily surmountable $\Delta G^{\ddagger}$s for the key elementary steps, namely, N_2 adsorption and reduction of $^{*}NH_2$ to $^{*}NH_3$.

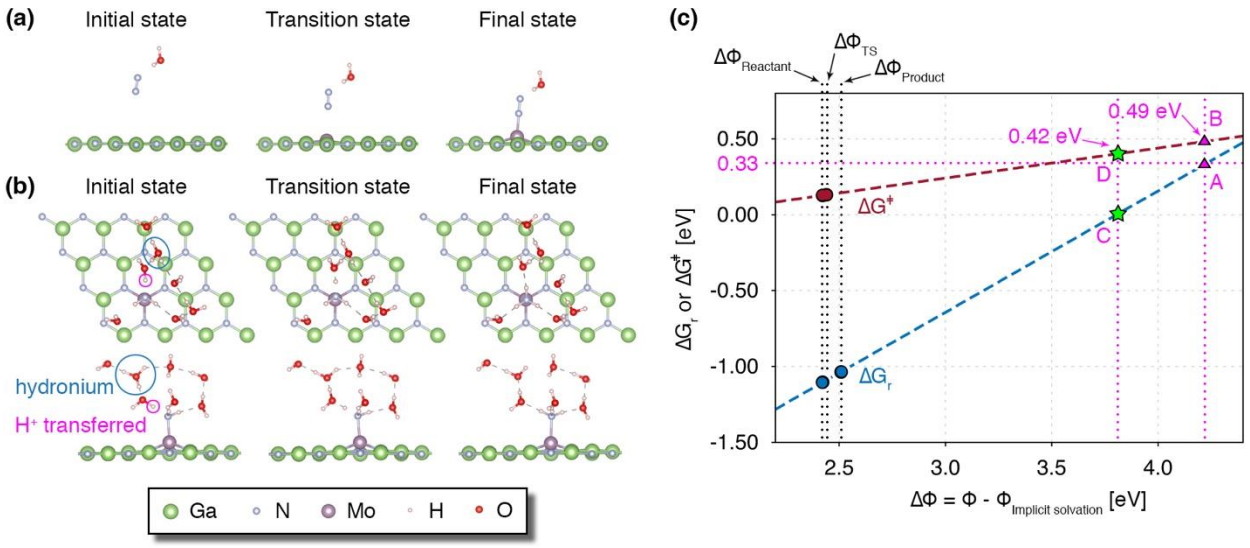

729

730 **Figure 7.** Geometries of the initial state, transition state, and final state for the elementary steps of
731 (a) N_2 adsorption via the preferred end-on configuration (side views) and (b) the PDS converting
732 $^*NH_2$ to $^*NH_3$ (top and side views), where the hydronium and the proton (H^+) that transfers to the
733 $^*NH_2$ are indicated by blue and magenta circles, respectively. (c) Predicted Gibbs free energies for
734 the PDS as a function of the (relative) surface potential or work function. Determined linear
735 relationship between reaction/activation Gibbs free energy ($\Delta G_r/\Delta G^{\ddagger}$) and the relative surface
736 potential with respect to implicit solvation ($\Delta\Phi$) are shown in blue/red dashed lines. Points A/B
737 and C/D respectively represent the $\Delta G_r/\Delta G^{\ddagger}$ of the PDS (step 7) at 0 V vs. the RHE and at the
738 onset potential through the distal pathway on the Mo@g-GaN monolayer (-0.41 V vs. the RHE,
739 derived by determining the needed shift in $\Delta\Phi$ from ΔG_r= 0.33 eV or point A, to ΔG_r= 0 eV or
740 point C).

741

742 3.6 Selectivity of the NRR on the Mo@g-GaN monolayer

743 The hydrogen evolution reaction (HER) is the key side reaction during the NRR that directly
744 consumes protons and electrons, leading to a low FE, i.e., selectivity, towards ammonia.[119-121]

Under typical experimental conditions, adsorption of H (reduction of aqueous protons) rather than protonation of $^{*}N_xH_y$ not only opens a path for the HER, but also, more importantly, blocks active sites on the surface of the electrocatalyst where the NRR process initiates. Therefore, the HER may reduce the selectivity toward ammonia and thus is considered to be the major competing reaction during the NRR.[122-123]

Adsorption selectivity is one way to improve overall NRR selectivity.[44,46,52] One can estimate this metric based on the Gibbs free energy difference between the two competing reactions of N_2 adsorption and single H atom adsorption, i.e., $\delta G = \Delta G_{ads}(N_2) - \Delta G_{ads}(H)$. We predict the single H atom adsorption Gibbs free energy ΔG_{ads}(H) on the Mo atom of the Mo@g-GaN monolayer to be -0.31 eV at 0 V vs. the RHE. Therefore, for the distal pathway with end-on adsorption of N_2, $\delta G = -0.67\ eV - (-0.31\ eV) = -0.36\ eV$. Such a δG value is much more negative than those found on penta-TiP (0.03 eV),[106] Ru(0001) (0.11 eV) and Ru/NC_2 (0.32 eV),[52] indicating that adsorption of N_2 dominates on the Mo@g-GaN monolayer over H adsorption at 0 V vs. the RHE. The operating potential to initiate the NRR (i.e., the distal pathway onset potential $U = -0.33\ V$ vs. the RHE) will facilitate H adsorption further while having no effect on N_2 adsorption, because the former is driven by a potential whereas the latter is not.[119] Therefore, we can use $\delta G^{onset} = \Delta G_{ads}(N_2) - \Delta G_{ads}^{onset}(H) = \Delta G_{ads}(N_2) - [\Delta G_{ads}(H) + U \cdot e]$ to describe the adsorption selectivity at the onset potential U of the NRR. For most of the SACs on 2D substrates investigated previously,[44,45,48,50,51,53] the δG is predicted to be negative at 0 V vs. the RHE. However, the surface of the electrocatalyst will be covered mainly by H at their corresponding NRR operating potentials (i.e., with a positive δG^{onset}), blocking active sites for the NRR. This has been suggested to be one of the fundamental reasons for the very low selectivity for the NRR under ambient conditions.[119] In our case, however, at the NRR onset potential for the

768 distal pathway, $\delta G^{onset} = \Delta G_{ads}(N_2) - \Delta G_{ads}^{onset}(H) = -0.67\ eV - (-0.31 - 0.33)\ eV =$
769 $-0.03\ eV$. Such an slightly negative δG^{onset}, given the uncertainties in our model, suggests that
770 adsorption of N_2 is at least competitive with the adsorption of H on the Mo@g-GaN monolayer
771 even at the NRR operating potential, leading to an expected improvement in adsorption selectivity
772 compared to earlier catalysts.

773 Another metric for NRR selectivity is the difference between the limiting potentials for the
774 NRR and HER, which can be calculated as

775 $$\Delta U = U_{PDS}(NRR) - U_{PDS}(HER),$$

776 where $U_{PDS}(NRR)$ and $U_{PDS}(HER)$ are the minimum potentials required to make all of the
777 electroactive steps for the NRR and HER spontaneous, respectively. In the present case,
778 $U_{PDS}(NRR) = -0.33\ V$, $U_{PDS}(HER) = -0.31\ V$. Therefore, $\Delta U = -0.33\ V - (-0.31\ V) =$
779 $-0.02\ V$, which is, although negative, significantly less so than those of metal-based benchmarks
780 (~ -0.5 V).[22] It is possible, then, that this monolayer will have a higher catalytic selectivity for
781 the NRR than the materials observed previously.[121] In addition, following Yang and co-workers,[46]
782 NRR catalytic selectivity also can be estimated from the Boltzmann distribution,

783 $$f_{NRR} = 1/\{1 + exp[(\Delta G_{PDS}(NRR) - \Delta G_{PDS}(HER))/k_B T]\},$$

784 where $\Delta G_{PDS}(NRR)$ and $\Delta G_{PDS}(HER)$ are the Gibbs free energy changes of the PDSs for the
785 NRR and HER, respectively, k_B is the Boltzmann constant, and T is the temperature (here, 298.15
786 K). f_{NRR} approximates the mole fraction of NH_3 in the total product stream (NH_3 + H_2). This
787 approximation assumes that the NRR and HER processes are rate-controlled only by their
788 respective PDS. According to the Boltzmann distribution, the NRR catalytic selectivity on the

789 Mo@g-GaN monolayer thus will be ~31% at room temperature. Such a selectivity is much higher
790 than values obtained in recent experiments on other substrates.[26,124-126]

791

792 4. SUMMARY AND CONCLUSIONS

793 In summary, by using spin-polarized DFT-PBE-D3 calculations and the CHE model, we
794 systematically investigated the ability of single TM atoms (Sc, Ti, V, Cr, Mn, Fe, Co, Ni, Cu, Zn,
795 Mo, Ru, Rh, Pd, and Ag) substitutionally doped into a g-GaN monolayer to act as electrocatalysts
796 for N_2 fixation into ammonia. To mimic an aqueous solution during the NRR, we employed a
797 mixed implicit + explicit solvation model in which explicit water molecules were included in the
798 first solvation shell, forming hydrogen bonds with the adsorbates, while an implicit (continuum)
799 solvent model captured longer-range solvation effects. Our calculations suggest that the Mo@g-
800 GaN monolayer exhibits exceptional NRR catalytic activity, where the NRR prefers a distal
801 pathway with a low onset potential of -0.33 V vs. the RHE, corresponding to a small overpotential
802 of 0.42 V vs. the RHE, referenced to the experimental equilibrium potential of 0.09 V vs. the RHE.
803 We further predicted a modest kinetic barrier for the PDS of 0.42 eV at the onset potential derived
804 from the kinetic analysis (-0.41 V vs. the RHE). Additionally, the Mo@g-GaN monolayer is
805 expected to exhibit higher selectivity (~31%) than previously achieved for NRR over the
806 competing HER process, even at the onset potential.

807 Multiple theoretical studies have predicted candidate SACs for artificial ammonia synthesis
808 via electrochemical NRR. The investigated substrates include numerous 2D materials, such as
809 boron nitride, nanoporous carbon, graphene-based materials, nitrogen-doped carbon, graphdiyne,
810 TM dichalcogenides, and graphitic carbon nitrides.[44-53] However, these previously proposed SACs
811 manifest relatively low selectivity for N_2 relative to H adsorption when compared to Mo@g-GaN.

Indeed, in the previously investigated SACs, even though the adsorption of H was found to be less favorable than N_2 adsorption at 0 V, the former is predicted to dominate under the operating voltage because of the very negative potential requirement of the PDS for NRR on these catalysts, enough to drive H adsorption.[44,45,48,50,51,53] In our case, however, adsorption of N_2 is at least competitive with the adsorption of H on the Mo@g-GaN monolayer even at the NRR operating potential, leading to an expected improvement in adsorption selectivity compared to earlier SACs. Furthermore, most of the previous theoretical studies did not investigate the stability of the proposed SACs as rigorously as in this work. We demonstrated the structural and chemical stability of the catalyst, evaluating the ability of Mo to remain in the g-GaN lattice, the chemical inertness of the lattice N toward hydrogenation (which should prevent incidental ammonia production from the catalyst itself), and the likely stability of the active site with respect to oxidation.

With respect to methodology, note that previous simulations aimed at designing electrocatalysts for NRR mostly neglected solvation effects, which was justified by a study that found implicit solvation changed the reaction energies by < 0.1 eV.[22] However, our more sophisticated implicit + explicit solvation model not only substantially changed Gibbs free energies (by as much as 0.86 eV, Figure S4c) but also altered the identity of the PDS (Figure S4b), which calls into question the results of those earlier, simpler simulations.

To conclude, our findings open up a new avenue for artificial ammonia synthesis via electrocatalytic reduction of nitrogen using single-atom catalysts embedded in semiconductor monolayers. The Mo@g-GaN monolayer proposed in this work is a promising candidate NRR electrocatalyst, deserving of future experimental validation.

AUTHOR INFORMATION

Corresponding Author

* eac@ucla.edu

Notes

The authors declare no competing financial interest.

Supporting Information

Test calculations for choosing the PAW potential for Mo based on N_2 adsorption energies; energy convergence with respect to kinetic energy cutoff and k-mesh; optimized geometry of the pristine graphene-like GaN (g-GaN) monolayer; plane-averaged electrostatic potentials along the surface normal for $^*NH_3$ on the Mo@g-GaN monolayer with and without dipole correction; deviation of lattice constants of the TM-doped g-GaN monolayers; finite size error introduced in the 4×4 supercell; reaction Gibbs free energies of each NRR elementary step using either implicit solvation or the mixed implicit + explicit solvation model; variation of the total energy and geometry snapshots of the Mo@g-GaN monolayer during 20-ps DFT-PBE-D3 molecular dynamics trajectories at 300, 500, and 1000 K; Gibbs free energy profile for diffusion for a single Mo atom from its anchoring site to a neighboring hollow site; structures and adsorption Gibbs free energies of H atoms adsorbed on lattice N sites of the Mo@g-GaN monolayer, the reaction Gibbs free energy profiles for forming NH_n by removing lattice N sites, as well as the optimized geometries of hydration and oxidation products of Mo@g-GaN, all via DFT-PBE-D3 and implicit solvation; spin down component of the pCOHP between the Mo atom and its nearest N atom in the adsorbed N_2; Gibbs free energy profile for dissociation of side-on adsorbed N_2; reaction Gibbs free energy diagrams for the NRR on the Mo@g-GaN monolayer via the mixed pathways; optimized geometries of the intermediates and reaction Gibbs free energies along the distal pathway from DFT-PBE-D3 with the mixed implicit +

explicit solvation model for the second set of water configurations; analysis of kinetic barrier calculations at constant potential in the presence of implicit solvent.

ACKNOWLEDGMENTS

E.A.C. thanks the U.S. Department of Energy, Office of Science, Basic Energy Sciences (Grant No. DE-SC0002120) for support of this work. We also thank Dr. Shenzhen Xu and Ms. Nari L. Baughman for a critical reading of an early draft of this paper. L.L. thanks Dr. Shenzhen Xu and Dr. Robert B. Wexler for fruitful discussions and Ms. Samantha Luu for proofreading a revised version of the paper.

REFERENCES

(1) Schlögl, R., Catalytic Synthesis of Ammonia—a "Never-Ending Story"? *Angew. Chem., Int. Ed.* **2003**, *42*, 2004-2008.

(2) Galloway, J. N.; Townsend, A. R.; Erisman, J. W.; Bekunda, M.; Cai, Z.; Freney, J. R.; Martinelli, L. A.; Seitzinger, S. P.; Sutton, M. A., Transformation of the Nitrogen Cycle: Recent Trends, Questions, and Potential Solutions. *Science* **2008**, *320*, 889-892.

(3) Rosca, V.; Duca, M.; de Groot, M. T.; Koper, M. T., Nitrogen Cycle Electrocatalysis. *Chem. Rev.* **2009**, *109*, 2209-2244.

(4) Christensen, C. H.; Johannessen, T.; Sørensen, R. Z.; Nørskov, J. K., Towards an Ammonia-Mediated Hydrogen Economy? *Catal. Today* **2006**, *111*, 140-144.

(5) Schüth, F.; Palkovits, R.; Schlögl, R.; Su, D. S., Ammonia as a Possible Element in an Energy Infrastructure: Catalysts for Ammonia Decomposition. *Energy Environ. Sci.* **2012**, *5*, 6278-6289.

(6) Gür, T. M., Review of Electrical Energy Storage Technologies, Materials and Systems: Challenges and Prospects for Large-Scale Grid Storage. *Energy Environ. Sci.* **2018**, *11*, 2696-2767.

(7) Honkala, K.; Hellman, A.; Remediakis, I.; Logadottir, A.; Carlsson, A.; Dahl, S.; Christensen, C. H.; Nørskov, J. K., Ammonia Synthesis from First-Principles Calculations. *Science* **2005**, *307*, 555-558.

(8) Légaré, M.-A.; Bélanger-Chabot, G.; Dewhurst, R. D.; Welz, E.; Krummenacher, I.; Engels, B.; Braunschweig, H., Nitrogen Fixation and Reduction at Boron. *Science* **2018**, *359*, 896-900.

(9) Appl, M., *Ammonia*. Wiley-VCH: Weinheim, Germany, 2006; p 1-155.

(10) Wang, L.; Xia, M.; Wang, H.; Huang, K.; Qian, C.; Maravelias, C. T.; Ozin, G. A., Greening Ammonia toward the Solar Ammonia Refinery. *Joule* **2018**, *2*, 1055-1074.

(11) Kitano, M.; Inoue, Y.; Yamazaki, Y.; Hayashi, F.; Kanbara, S.; Matsuishi, S.; Yokoyama, T.; Kim, S.-W.; Hara, M.; Hosono, H., Ammonia Synthesis Using a Stable Electride as an Electron Donor and Reversible Hydrogen Store. *Nat. Chem.* **2012**, *4*, 934.

(12) Van der Ham, C. J.; Koper, M. T.; Hetterscheid, D. G., Challenges in Reduction of Dinitrogen by Proton and Electron Transfer. *Chem. Soc. Rev.* **2014**, *43*, 5183-5191.

(13) Daims, H.; Lebedeva, E. V.; Pjevac, P.; Han, P.; Herbold, C.; Albertsen, M.; Jehmlich, N.; Palatinszky, M.; Vierheilig, J.; Bulaev, A., Complete Nitrification by Nitrospira Bacteria. *Nature* **2015**, *528*, 504.

(14) Martín, A. J.; Shinagawa, T.; Pérez-Ramírez, J., Electrocatalytic Reduction of Nitrogen: From Haber-Bosch to Ammonia Artificial Leaf. *Chem* **2019**, *5*, 263-283.

(15) Van Kessel, M. A.; Speth, D. R.; Albertsen, M.; Nielsen, P. H.; den Camp, H. J. O.; Kartal, B.; Jetten, M. S.; Lücker, S., Complete Nitrification by a Single Microorganism. *Nature* **2015**, *528*, 555.

(16) Shi, M. M.; Bao, D.; Wulan, B. R.; Li, Y. H.; Zhang, Y. F.; Yan, J. M.; Jiang, Q., Au Sub-Nanoclusters on TiO_2 toward Highly Efficient and Selective Electrocatalyst for N_2 Conversion to NH_3 at Ambient Conditions. *Adv. Materials* **2017**, *29*, 1606550.

(17) Pool, J. A.; Lobkovsky, E.; Chirik, P. J., Hydrogenation and Cleavage of Dinitrogen to Ammonia with a Zirconium Complex. *Nature* **2004**, *427*, 527.

(18) Kandemir, T.; Schuster, M. E.; Senyshyn, A.; Behrens, M.; Schlögl, R., The Haber–Bosch Process Revisited: On the Real Structure and Stability of "Ammonia Iron" under Working Conditions. *Angew. Chem., Int. Ed.* **2013**, *52*, 12723-12726.

(19) Chen, X.; Li, N.; Kong, Z.; Ong, W.-J.; Zhao, X., Photocatalytic Fixation of Nitrogen to Ammonia: State-of-the-Art Advancements and Future Prospects. *Mater. Horiz.* **2018**, *5*, 9-27.

(20) Li, M.; Huang, H.; Low, J.; Gao, C.; Long, R.; Xiong, Y., Recent Progress on Electrocatalyst and Photocatalyst Design for Nitrogen Reduction. *Small Methods* **2018**, 1800388.

(21) Milton, R. D.; Cai, R.; Abdellaoui, S.; Leech, D.; De Lacey, A. L.; Pita, M.; Minteer, S. D., Bioelectrochemical Haber–Bosch Process: An Ammonia-Producing H_2/N_2 Fuel Cell. *Angew. Chem., Int. Ed.* **2017**, *56*, 2680-2683.

(22) Montoya, J. H.; Tsai, C.; Vojvodic, A.; Nørskov, J. K., The Challenge of Electrochemical Ammonia Synthesis: A New Perspective on the Role of Nitrogen Scaling Relations. *ChemSusChem* **2015**, *8*, 2180-2186.

(23) Jia, H.-P.; Quadrelli, E. A., Mechanistic Aspects of Dinitrogen Cleavage and Hydrogenation to Produce Ammonia in Catalysis and Organometallic Chemistry: Relevance of Metal Hydride Bonds and Dihydrogen. *Chem. Soc. Rev.* **2014**, *43*, 547-564.

(24) Burford, R. J.; Fryzuk, M. D., Examining the Relationship between Coordination Mode and Reactivity of Dinitrogen. *Nat. Rev. Chem.* **2017**, *1*, 0026.

(25) Liu, Y.; Su, Y.; Quan, X.; Fan, X.; Chen, S.; Yu, H.; Zhao, H.; Zhang, Y.; Zhao, J., Facile Ammonia Synthesis from Electrocatalytic N_2 Reduction under Ambient Conditions on N-Doped Porous Carbon. *ACS Catal.* **2018**, *8*, 1186-1191.

(26) Qin, Q.; Heil, T.; Antonietti, M.; Oschatz, M., Single-Site Gold Catalysts on Hierarchical N-Doped Porous Noble Carbon for Enhanced Electrochemical Reduction of Nitrogen. *Small Methods* **2018**, *2*, 1800202.

(27) Scepaniak, J. J.; Young, J. A.; Bontchev, R. P.; Smith, J. M., Formation of Ammonia from an Iron Nitrido Complex. *Angew. Chem., Int. Ed.* **2009**, *48*, 3158-3160.

(28) Rittle, J.; Peters, J. C., An Fe-N_2 Complex That Generates Hydrazine and Ammonia Via Fe=NNH_2: Demonstrating a Hybrid Distal-to-Alternating Pathway for N_2 Reduction. *J. Am. Chem. Soc.* **2016**, *138*, 4243-4248.

(29) Eizawa, A.; Arashiba, K.; Tanaka, H.; Kuriyama, S.; Matsuo, Y.; Nakajima, K.; Yoshizawa, K.; Nishibayashi, Y., Remarkable Catalytic Activity of Dinitrogen-Bridged Dimolybdenum Complexes Bearing NHC-Based PCP-Pincer Ligands toward Nitrogen Fixation. *Nat. Commun.* **2017**, *8*, 14874.

(30) Fajardo Jr, J.; Peters, J. C., Catalytic Nitrogen-to-Ammonia Conversion by Osmium and Ruthenium Complexes. *J. Am. Chem. Soc.* **2017**, *139*, 16105-16108.

(31) Sekiguchi, Y.; Kuriyama, S.; Eizawa, A.; Arashiba, K.; Nakajima, K.; Nishibayashi, Y., Synthesis and Reactivity of Iron–Dinitrogen Complexes Bearing Anionic Methyl-and Phenyl-Substituted Pyrrole-Based PNP-Type Pincer Ligands toward Catalytic Nitrogen Fixation. *Chem. Commun.* **2017**, *53*, 12040-12043.

(32) Thompson, N. B.; Green, M. T.; Peters, J. C., Nitrogen Fixation Via a Terminal Fe (IV) Nitride. *J. Am. Chem. Soc.* **2017**, *139*, 15312-15315.

(33) Tyo, E. C.; Vajda, S., Catalysis by Clusters with Precise Numbers of Atoms. *Nat. Nanotechnol.* **2015**, *10*, 577-588.

(34) Fan, L.; Liu, P. F.; Yan, X.; Gu, L.; Yang, Z. Z.; Yang, H. G.; Qiu, S.; Yao, X., Atomically Isolated Nickel Species Anchored on Graphitized Carbon for Efficient Hydrogen Evolution Electrocatalysis. *Nat. Commun.* **2016**, *7*, 10667.

(35) Gao, G.; Jiao, Y.; Waclawik, E. R.; Du, A., Single Atom (Pd/Pt) Supported on Graphitic Carbon Nitride as an Efficient Photocatalyst for Visible-Light Reduction of Carbon Dioxide. *J. Am. Chem. Soc.* **2016**, *138*, 6292-6297.

(36) Yin, C.; Negreiros, F. R.; Barcaro, G.; Beniya, A.; Sementa, L.; Tyo, E. C.; Bartling, S.; Meiwes-Broer, K.-H.; Seifert, S.; Hirata, H., Alumina-Supported Sub-Nanometer Pt_{10} Clusters: Amorphization and Role of the Support Material in a Highly Active CO Oxidation Catalyst. *J. Mater. Chem. A* **2017**, *5*, 4923-4931.

(37) Zhu, C.; Fu, S.; Shi, Q.; Du, D.; Lin, Y., Single-Atom Electrocatalysts. *Angew. Chem., Int. Ed.* **2017**, *56*, 13944-13960.

(38) Zhang, L.; Jia, Y.; Gao, G.; Yan, X.; Chen, N.; Chen, J.; Soo, M. T.; Wood, B.; Yang, D.; Du, A., Graphene Defects Trap Atomic Ni Species for Hydrogen and Oxygen Evolution Reactions. *Chem* **2018**, *4*, 285-297.

(39) Qiao, B.; Wang, A.; Yang, X.; Allard, L. F.; Jiang, Z.; Cui, Y.; Liu, J.; Li, J.; Zhang, T., Single-Atom Catalysis of CO Oxidation Using Pt_1/FeO_x. *Nat. Chem.* **2011**, *3*, 634.

(40) Yang, X.-F.; Wang, A.; Qiao, B.; Li, J.; Liu, J.; Zhang, T., Single-Atom Catalysts: A New Frontier in Heterogeneous Catalysis. *Acc. Chem. Res.* **2013**, *46*, 1740-1748.

(41) Lucci, F. R.; Liu, J.; Marcinkowski, M. D.; Yang, M.; Allard, L. F.; Flytzani-Stephanopoulos, M.; Sykes, E. C. H., Selective Hydrogenation of 1, 3-Butadiene on Platinum–Copper Alloys at the Single-Atom Limit. *Nat. Commun.* **2015**, *6*, 8550.

(42) Thomas, J. M., Catalysis: Tens of Thousands of Atoms Replaced by One. *Nature* **2015**, *525*, 325.

(43) Yan, H.; Cheng, H.; Yi, H.; Lin, Y.; Yao, T.; Wang, C.; Li, J.; Wei, S.; Lu, J., Single-Atom Pd_1/Graphene Catalyst Achieved by Atomic Layer Deposition: Remarkable Performance in Selective Hydrogenation of 1, 3-Butadiene. *J. Am. Chem. Soc.* **2015**, *137*, 10484-10487.

(44) Zhao, J.; Chen, Z., Single Mo Atom Supported on Defective Boron Nitride Monolayer as an Efficient Electrocatalyst for Nitrogen Fixation: A Computational Study. *J. Am. Chem. Soc.* **2017**, *139*, 12480-12487.

(45) Cao, Y.; Gao, Y.; Zhou, H.; Chen, X.; Hu, H.; Deng, S.; Zhong, X.; Zhuang, G.; Wang, J., Highly Efficient Ammonia Synthesis Electrocatalyst: Single Ru Atom on Naturally Nanoporous Carbon Materials. *Adv. Theory Simul.* **2018**, *1*, 1870012.

(46) Zhao, W.; Zhang, L.; Luo, Q.; Hu, Z.; Zhang, W.; Smith, S.; Yang, J., Single $Mo_1(Cr_1)$ Atom on Nitrogen-Doped Graphene Enables Highly Selective Electroreduction of Nitrogen into Ammonia. *ACS Catal.* **2019**, *9*, 3419-3425.

(47) Liu, X.; Jiao, Y.; Zheng, Y.; Jaroniec, M.; Qiao, S.-Z., Building up a Picture of the Electrocatalytic Nitrogen Reduction Activity of Transition Metal Single-Atom Catalysts. *J. Am. Chem. Soc.* **2019**, *141*, 9664-9672.

(48) Han, X. Q.; Lang, Z. L.; Yan, L. L.; Guan, W.; Ci, C. G.; Su, Z. M., Atomic Nb Anchoring on Graphdiyne as a New Potential Electrocatalyst for Nitrogen Fixation: A Computational View. *Adv. Theory Simul.* **2019**, *2*, 1900132

(49) Zhang, J.; Tian, X.; Liu, M.; Guo, H.; Zhou, J.; Fang, Q.; Liu, Z.; Wu, Q.; Lou, J., Cobalt-Modulated Molybdenum–Dinitrogen Interaction in MoS_2 for Catalyzing Ammonia Synthesis. *J. Am. Chem. Soc.* **2019**, *141*, 19269-19275.

(50) Chen, Z.; Zhao, J.; Cabrera, C. R.; Chen, Z., Computational Screening of Efficient Single-Atom Catalysts Based on Graphitic Carbon Nitride (g-C_3N_4) for Nitrogen Electroreduction. *Small Methods* **2018**, 1800368.

(51) Wang, Z.; Yu, Z.; Zhao, J., Computational Screening of a Single Transition Metal Atom Supported on the C_2N Monolayer for Electrochemical Ammonia Synthesis. *Phys. Chem. Chem. Phys.* **2018**, *20*, 12835-12844.

(52) Tao, H.; Choi, C.; Ding, L.-X.; Jiang, Z.; Han, Z.; Jia, M.; Fan, Q.; Gao, Y.; Wang, H.; Robertson, A. W.; Hong, S.; Jung, Y.; Liu, S.; Sun, Z., Nitrogen Fixation by Ru Single-Atom Electrocatalytic Reduction. *Chem* **2019**, *5*, 204-214.

(53) Yin, H.; Li, S.-L.; Gan, L.-Y.; Wang, P., Pt-Embedded in Monolayer g-C_3N_4 as a Promising Single-Atom Electrocatalyst for Ammonia Synthesis. *J. Mater. Chem. A* **2019**, *7*, 11908-11914.

(54) Zhuang, H. L.; Singh, A. K.; Hennig, R. G., Computational Discovery of Single-Layer III-V Materials. *Phys. Rev. B* **2013**, *87*, 165415.

(55) Singh, A. K.; Zhuang, H. L.; Hennig, R. G., Ab Initio Synthesis of Single-Layer III-V Materials. *Phys. Rev. B* **2014**, *89*, 245431.

(56) Al Balushi, Z. Y.; Wang, K.; Ghosh, R. K.; Vilá, R. A.; Eichfeld, S. M.; Caldwell, J. D.; Qin, X.; Lin, Y.-C.; DeSario, P. A.; Stone, G., Two-Dimensional Gallium Nitride Realized Via Graphene Encapsulation. *Nat. Mater.* **2016**, *15*, 1166.

(57) Liu, B.; Yang, W.; Li, J.; Zhang, X.; Niu, P.; Jiang, X., Template Approach to Crystalline Gan Nanosheets. *Nano Lett.* **2017**, *17*, 3195-3201.

(58) Sun, C.; Yang, M.; Wang, T.; Shao, Y.; Wu, Y.; Hao, X., Graphene-Oxide-Assisted Synthesis of Gan Nanosheets as a New Anode Material for Lithium-Ion Battery. *ACS Appl. Mater. Interfaces* **2017**, *9*, 26631-26636.

(59) Li, L.; Wang, Y.; Vanka, S.; Mu, X.; Mi, Z.; Li, C. J., Nitrogen Photofixation over III-Nitride Nanowires Assisted by Ruthenium Clusters of Low Atomicity. *Angew. Chem., Int. Ed.* **2017**, *56*, 8701-8705.

(60) Kresse, G.; Furthmüller, J., Efficiency of Ab-Initio Total Energy Calculations for Metals and Semiconductors Using a Plane-Wave Basis Set. *Comput. Mater. Sci.* **1996**, *6*, 15-50.

(61) Kresse, G.; Furthmüller, J., Efficient Iterative Schemes for Ab Initio Total-Energy Calculations Using a Plane-Wave Basis Set. *Phys. Rev. B* **1996**, *54*, 11169-11186.

(62) Kresse, G.; Joubert, D., From Ultrasoft Pseudopotentials to the Projector Augmented-Wave Method. *Phys. Rev. B* **1999**, *59*, 1758-1775.

(63) Blöchl, P. E., Projector Augmented-Wave Method. *Phys. Rev. B* **1994**, *50*, 17953.

(64) Perdew, J. P.; Burke, K.; Ernzerhof, M., Generalized Gradient Approximation Made Simple. *Phys. Rev. Lett.* **1996**, *77*, 3865-3868.

(65) Grimme, S.; Antony, J.; Ehrlich, S.; Krieg, H., A Consistent and Accurate Ab Initio Parametrization of Density Functional Dispersion Correction (DFT-D) for the 94 Elements H-Pu. *J. Chem. Phys.* **2010**, *132*, 154104.

(66) Grimme, S.; Ehrlich, S.; Goerigk, L., Effect of the Damping Function in Dispersion Corrected Density Functional Theory. *J. Comput. Chem.* **2011**, *32*, 1456-1465.

(67) Monkhorst, H. J.; Pack, J. D., Special Points for Brillouin-Zone Integrations. *Phys. Rev. B* **1976**, *13*, 5188-5192.

(68) Monemar, B., Fundamental Energy Gap of Gan from Photoluminescence Excitation Spectra. *Phys. Rev. B* **1974**, *10*, 676.

(69) Schulz, H.; Thiemann, K., Crystal Structure Refinement of AlN and GaN. *Solid State Commun.* **1977**, *23*, 815-819.

(70) Li, H.; Dai, J.; Li, J.; Zhang, S.; Zhou, J.; Zhang, L.; Chu, W.; Chen, D.; Zhao, H.; Yang, J.; Wu, Z., Electronic Structures and Magnetic Properties of GaN Sheets and Nanoribbons. *J. Phys. Chem. C* **2010**, *114*, 11390-11394.

(71) Blonsky, M. N.; Zhuang, H. L.; Singh, A. K.; Hennig, R. G., Ab Initio Prediction of Piezoelectricity in Two-Dimensional Materials. *ACS Nano* **2015**, *9*, 9885-9891.

(72) Camacho-Mojica, D. C.; López-Urías, F., Gan Haeckelite Single-Layered Nanostructures: Monolayer and Nanotubes. *Sci. Rep.* **2015**, *5*, 17902.

(73) Lewis, D. K.; Matsubara, M.; Bellotti, E.; Sharifzadeh, S., Quasiparticle and Hybrid Density Functional Methods in Defect Studies: An Application to the Nitrogen Vacancy in GaN. *Phys. Rev. B* **2017**, *96*, 235203.

(74) Prete, M. S.; Mosca Conte, A.; Gori, P.; Bechstedt, F.; Pulci, O., Tunable Electronic Properties of Two-Dimensional Nitrides for Light Harvesting Heterostructures. *Appl. Phys. Lett.* **2017**, *110*, 012103.

(75) Zhang, H.; Meng, F.-S.; Wu, Y.-B., Two Single-Layer Porous Gallium Nitride Nanosheets: A First-Principles Study. *Solid State Commun.* **2017**, *250*, 18-22.

(76) Lucking, M. C.; Xie, W.; Choe, D.-H.; West, D.; Lu, T.-M.; Zhang, S., Traditional Semiconductors in the Two-Dimensional Limit. *Phys. Rev. Lett.* **2018**, *120*, 086101.

(77) Guo, Y.; Zhu, H.; Wang, Q., Piezoelectric Effects in Surface-Engineered Two-Dimensional Group III Nitrides. *ACS Appl. Mater. Interfaces* **2019**, *11*, 1033-1039.

(78) Henkelman, G.; Uberuaga, B. P.; Jónsson, H. A Climbing Image Nudged Elastic Band Method for Finding Saddle Points and Minimum Energy Paths. *J. Chem. Phys.* **2000**, *113*, 9901-9904.

(79) Liechtenstein, A. I.; Anisimov, V. I.; Zaanen, J., Density-Functional Theory and Strong Interactions: Orbital Ordering in Mott-Hubbard Insulators. *Phys. Rev. B* **1995**, *52*, R5467-R5470.

(80) Dudarev, S. L.; Botton, G. A.; Savrasov, S. Y.; Humphreys, C. J.; Sutton, A. P., Electron-Energy-Loss Spectra and the Structural Stability of Nickel Oxide: An LSDA+U Study. *Phys. Rev. B* **1998**, *57*, 1505-1509.

(81) Vaugier, L.; Jiang, H.; Biermann, S., Hubbard U and Hund Exchange J in Transition Metal Oxides: Screening Versus Localization Trends from Constrained Random Phase Approximation. *Phys. Rev. B* **2012**, *86*, 165105.

(82) Dronskowski, R.; Bloechl, P. E., Crystal Orbital Hamilton Populations (COHP): Energy-Resolved Visualization of Chemical Bonding in Solids Based on Density-Functional Calculations. *J. Phys. Chem.* **1993**, *97*, 8617-8624.

(83) Deringer, V. L.; Tchougréeff, A. L.; Dronskowski, R., Crystal Orbital Hamilton Population (COHP) Analysis as Projected from Plane-Wave Basis Sets. *J. Phys. Chem. A* **2011**, *115*, 5461-5466.

(84) Maintz, S.; Deringer, V. L.; Tchougréeff, A. L.; Dronskowski, R., Analytic Projection from Plane-Wave and PAW Wavefunctions and Application to Chemical-Bonding Analysis in Solids. *J. Comput. Chem.* **2013**, *34*, 2557-2567.

(85) Maintz, S.; Deringer, V. L.; Tchougréeff, A. L.; Dronskowski, R., Lobster: A Tool to Extract Chemical Bonding from Plane-Wave Based Dft. *J. Comput. Chem.* **2016**, *37*, 1030-1035.

(86) Fishman, M.; Zhuang, H. L.; Mathew, K.; Dirschka, W.; Hennig, R. G., Accuracy of Exchange-Correlation Functionals and Effect of Solvation on the Surface Energy of Copper. *Phys. Rev. B* **2013**, *87*, 245402.

(87) Mathew, K.; Sundararaman, R.; Letchworth-Weaver, K.; Arias, T.; Hennig, R. G., Implicit Solvation Model for Density-Functional Study of Nanocrystal Surfaces and Reaction Pathways. *J. Chem. Phys.* **2014**, *140*, 084106.

(88) Senftle, T. P.; Lessio, M.; Carter, E. A., Interaction of Pyridine and Water with the Reconstructed Surfaces of GaP(111) and CdTe(111) Photoelectrodes: Implications for CO_2 Reduction. *Chem. Mater.* **2016**, *28*, 5799-5810.

(89) Lessio, M.; Senftle, T. P.; Carter, E. A., Hydride Shuttle Formation and Reaction with CO_2 on GaP (110). *ChemSusChem* **2018**, *11*, 1558-1566.

(90) Kibria, M. G.; Edwards, J. P.; Gabardo, C. M.; Dinh, C. T.; Seifitokaldani, A.; Sinton, D.; Sargent, E. H., Electrochemical CO_2 Reduction into Chemical Feedstocks: From Mechanistic Electrocatalysis Models to System Design. *Adv. Materials* **2019**, 1807166.

(91) Computational Chemistry Comparison and Benchmark Database. http://cccbdb.nist.gov/.

(92) Nørskov, J. K.; Rossmeisl, J.; Logadottir, A.; Lindqvist, L.; Kitchin, J. R.; Bligaard, T.; Jonsson, H., Origin of the Overpotential for Oxygen Reduction at a Fuel-Cell Cathode. *J. Phys. Chem. B* **2004**, *108*, 17886-17892.

(93) Rossmeisl, J.; Logadottir, A.; Nørskov, J. K., Electrolysis of Water on (Oxidized) Metal Surfaces. *Chem. Phys.* **2005**, *319*, 178-184.

(94) Peterson, A. A.; Abild-Pedersen, F.; Studt, F.; Rossmeisl, J.; Nørskov, J. K., How Copper Catalyzes the Electroreduction of Carbon Dioxide into Hydrocarbon Fuels. *Energy Environ. Sci.* **2010**, *3*, 1311-1315.

(95) Skulason, E.; Bligaard, T.; Gudmundsdóttir, S.; Studt, F.; Rossmeisl, J.; Abild-Pedersen, F.; Vegge, T.; Jonsson, H.; Nørskov, J. K., A Theoretical Evaluation of Possible Transition Metal Electro-Catalysts for N_2 Reduction. *Phys. Chem. Chem. Phys.* **2012**, *14*, 1235-1245.

(96) Lindley, B. M.; Appel, A. M.; Krogh-Jespersen, K.; Mayer, J. M.; Miller, A. J. M., Evaluating the Thermodynamics of Electrocatalytic N_2 Reduction in Acetonitrile. *ACS Energy Lett.* **2016**, *1*, 698-704.

(97) Henkelman, G.; Arnaldsson, A.; Jónsson, H., A Fast and Robust Algorithm for Bader Decomposition of Charge Density. *Comput. Mater. Sci.* **2006**, *36*, 354-360.

(98) Sanville, E.; Kenny, S. D.; Smith, R.; Henkelman, G., Improved Grid-Based Algorithm for Bader Charge Allocation. *J. Comput. Chem.* **2007**, *28*, 899-908.

(99) Tang, W.; Sanville, E.; Henkelman, G., A Grid-Based Bader Analysis Algorithm without Lattice Bias. *J. Phys.: Condens. Matter* **2009**, *21*, 084204.

(100) Shannon, R. D., Revised Effective Ionic Radii and Systematic Studies of Interatomic Distances in Halides and Chalcogenides. *Acta crystallographica section A: crystal physics, diffraction, theoretical and general crystallography* **1976**, *32*, 751-767.

(101)Chen, P. C.; Hsieh, S. J.; Chen, C. C.; Zou, J., The Microstructure and Capacitance Characterizations of Anodic Titanium Based Alloy Oxide Nanotube. *J. Nanomater.* **2013**, *2013*, 73.

(102)Bard, A. J., Parsons, R. and Jordan, J., *Standard Potentials in Aqueous Solution*. IUPAC-Marcel Dekker Inc., New York: 1985; p 474.

(103)Nosé, S., A Unified Formulation of the Constant Temperature Molecular Dynamics Methods. *J. Chem. Phys.* **1984**, *81*, 511-519.

(104)Hoover, W. G., Canonical Dynamics: Equilibrium Phase-Space Distributions. *Phys. Rev. A* **1985**, *31*, 1695-1697.

(105)Chen, Z.; Zhao, J.; Yin, L.; Chen, Z., B-Terminated (111) Polar Surfaces of BP and BAs: Promising Metal-Free Electrocatalysts with Large Reaction Regions for Nitrogen Fixation. *J. Mater. Chem. A* **2019**, 7, 13284.

(106)Ying, Y.; Fan, K.; Luo, X.; Huang, H., Predicting Two-Dimensional Pentagonal Transition Metal Monophosphides for Efficient Electrocatalytic Nitrogen Reduction. *J. Mater. Chem. A* **2019**, *7*, 11444-11451.

(107)Yang, X.; Nash, J.; Anibal, J.; Dunwell, M.; Kattel, S.; Stavitski, E.; Attenkofer, K.; Chen, J. G.; Yan, Y.; Xu, B., Mechanistic Insights into Electrochemical Nitrogen Reduction Reaction on Vanadium Nitride Nanoparticles. *J. Am. Chem. Soc.* **2018**, *140*, 13387-13391.

(108)Andersen, S. Z.; Čolić, V.; Yang, S.; Schwalbe, J. A.; Nielander, A. C.; McEnaney, J. M.; Enemark-Rasmussen, K.; Baker, J. G.; Singh, A. R.; Rohr, B. A.; Statt, M. J.; Blair, S. J.; Mezzavilla, S.; Kibsgaard, J.; Vesborg, P. C. K.; Cargnello, M.; Bent, S. F.; Jaramillo, T. F.; Stephens, I. E. L.; Nørskov, J. K.; Chorkendorff, I., A Rigorous Electrochemical Ammonia Synthesis Protocol with Quantitative Isotope Measurements. *Nature* **2019**, *570*, 504-508.

(109) Hu, B.; Hu, M.; Seefeldt, L.; Liu, T. L., Electrochemical Dinitrogen Reduction to Ammonia by Mo_2N: Catalysis or Decomposition? *ACS Energy Lett.* **2019**, *4*, 1053-1054.

(110) Kibsgaard, J.; Nørskov, J. K.; Chorkendorff, I., The Difficulty of Proving Electrochemical Ammonia Synthesis. *ACS Energy Lett.* **2019**, *4*, 2986-2988.

(111) Li, L.; Tang, C.; Yao, D.; Zheng, Y.; Qiao, S.-Z., Electrochemical Nitrogen Reduction: Identification and Elimination of Contamination in Electrolyte. *ACS Energy Lett.* **2019**, *4*, 2111-2116.

(112) Lv, X.; Wei, W.; Li, F.; Huang, B.; Dai, Y., Metal-Free B@g-CN: Visible/Infrared Light-Driven Single Atom Photocatalyst Enables Spontaneous Dinitrogen Reduction to Ammonia. *Nano Lett.* **2019**, *19*, 6391-6399.

(113) Abghoui, Y.; Garden, A. L.; Hlynsson, V. F.; Björgvinsdóttir, S.; Ólafsdóttir, H.; Skúlason, E., Enabling Electrochemical Reduction of Nitrogen to Ammonia at Ambient Conditions through Rational Catalyst Design. *Phys. Chem. Chem. Phys.* **2015**, *17*, 4909-4918.

(114) Anderson, J. S.; Rittle, J.; Peters, J. C., Catalytic Conversion of Nitrogen to Ammonia by an Iron Model Complex. *Nature* **2013**, *501*, 84.

(115) Anderson, J. S.; Cutsail III, G. E.; Rittle, J.; Connor, B. A.; Gunderson, W. A.; Zhang, L.; Hoffman, B. M.; Peters, J. C., Characterization of an $Fe{\equiv}N{-}NH_2$ Intermediate Relevant to Catalytic N_2 Reduction to NH_3. *J. Am. Chem. Soc.* **2015**, *137*, 7803-7809.

(116) Del Castillo, T. J.; Thompson, N. B.; Peters, J. C., A Synthetic Single-Site Fe Nitrogenase: High Turnover, Freeze-Quench ^{57}Fe MöSsbauer Data, and a Hydride Resting State. *J. Am. Chem. Soc.* **2016**, *138*, 5341-5350.

(117) Chan, K.; Nørskov, J. K., Electrochemical Barriers Made Simple. *J. Phys. Chem. Lett.* **2015**, *6*, 2663-2668.

(118) Chan, K.; Nørskov, J. K., Potential Dependence of Electrochemical Barriers from Ab Initio Calculations. *J. Phys. Chem. Lett.* **2016**, *7*, 1686-1690.

(119) Singh, A. R.; Rohr, B. A.; Schwalbe, J. A.; Cargnello, M.; Chan, K.; Jaramillo, T. F.; Chorkendorff, I.; Nørskov, J. K., Electrochemical Ammonia Synthesis—the Selectivity Challenge. *ACS Catal.* **2017**, *7*, 706-709.

(120) Liu, C.; Li, Q.; Zhang, J.; Jin, Y.; MacFarlane, D. R.; Sun, C., Theoretical Evaluation of Possible 2D Boron Monolayer in N_2 Electrochemical Conversion into Ammonia. *J. Phys. Chem. C* **2018**, *122*, 25268-25273.

(121) Ling, C.; Ouyang, Y.; Li, Q.; Bai, X.; Mao, X.; Du, A.; Wang, J., A General Two-Step Strategy–Based High-Throughput Screening of Single Atom Catalysts for Nitrogen Fixation. *Small Methods* **2019**, *3*, 1800376.

(122) Seh, Z. W.; Kibsgaard, J.; Dickens, C. F.; Chorkendorff, I.; Nørskov, J. K.; Jaramillo, T. F., Combining Theory and Experiment in Electrocatalysis: Insights into Materials Design. *Science* **2017**, *355*, eaad4998.

(123) Guo, C.; Ran, J.; Vasileff, A.; Qiao, S.-Z., Rational Design of Electrocatalysts and Photo(Electro)Catalysts for Nitrogen Reduction to Ammonia (NH_3) under Ambient Conditions. *Energy Environ. Sci.* **2018**, *11*, 45-56.

(124) Geng, Z.; Liu, Y.; Kong, X.; Li, P.; Li, K.; Liu, Z.; Du, J.; Shu, M.; Si, R.; Zeng, J., Achieving a Record-High Yield Rate of 120.9 $\mu g_{NH_3} mg_{cat.}^{-1} h^{-1}$ for N_2 Electrochemical Reduction over Ru Single-Atom Catalysts. *Adv. Materials* **2018**, *30*, 1803498.

(125) Han, L.; Liu, X.; Chen, J.; Lin, R.; Liu, H.; Lü, F.; Bak, S.; Liang, Z.; Zhao, S.; Stavitski, E.; Luo, J.; Adzic, R. R.; Xin, H. L., Atomically Dispersed Molybdenum Catalysts for Efficient Ambient Nitrogen Fixation. *Angew. Chem., Int. Ed.* **2019**, *58*, 2321-2325.

(126)Song, P.; Wang, H.; Kang, L.; Ran, B.; Song, H.; Wang, R., Electrochemical Nitrogen Reduction to Ammonia at Ambient Conditions on Nitrogen and Phosphorus Co-Doped Porous Carbon. *Chem. Commun.* **2019**, *55*, 687-690.
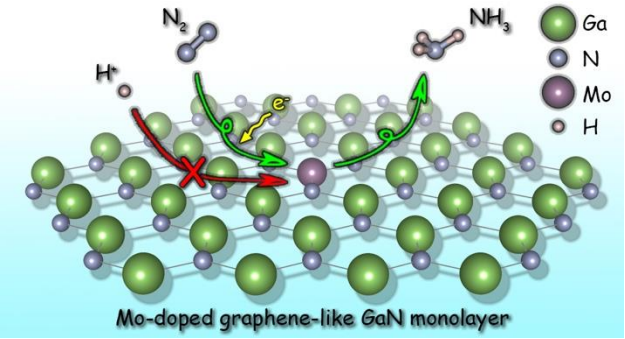
TOC